

1 **Past and future of the Arctic sea ice in HighResMIP climate** 2 **models**

3 Julia Selivanova^{1,2}, Doroteaciro Iovino¹, Francesco Cocetta¹

4 ¹ CMCC Foundation - Euro-Mediterranean Center on Climate Change, Italy

5 ² University of Bologna, Department of Physics and Astronomy, Bologna, Italy

6

7 *Correspondence to:* Julia Selivanova (julia.selivanova@cmcc.it)

8 **Abstract.**

9 We examine the past and projected changes in Arctic sea ice properties in 6 climate models participating in the High
10 Resolution Model Intercomparison Project (HighResMIP) in the Coupled Model Intercomparison Project Phase 6 (CMIP6).
11 Within HighResMIP each of the experiments are run using a reference resolution configuration (consistent with typical
12 CMIP6 runs) and higher resolution configurations. The role of horizontal grid resolution in both the atmosphere and ocean
13 model components in reproducing past and future changes in the Arctic sea ice cover is analysed. Model outputs from the
14 coupled historical (hist-1950) and future (highres-future) runs are used to describe the multi-model, multi-resolution
15 representation of the Arctic sea ice and to evaluate the systematic differences (if any) that resolution enhancement causes.
16 Our results indicate that there is not a strong relationship between the representation of sea ice cover and the
17 ocean/atmosphere grids; the impact of horizontal resolution depends rather on the examined sea ice characteristic and the
18 model used. However, the refinement of the ocean grid has a more prominent effect compared to the atmospheric one, with
19 eddy-permitting ocean configurations providing generally more realistic representations of sea ice area and sea ice edge. All
20 models project substantial sea ice shrinking: the Arctic loses nearly 95% of sea ice volume from 1950 to 2050. The model
21 selection based on historical performance potentially improves the accuracy of the model projections and predicts the Arctic
22 to turn ice-free as early as in 2047. Along with the overall sea ice loss, changes in the spatial structure of the total sea ice and
23 its partition in ice classes are noticed: the marginal ice zone (MIZ) will dominate the ice cover by 2050 suggesting a shift to
24 a new sea ice regime much closer to the current Antarctic sea ice conditions. The MIZ-dominated Arctic might drive
25 developments and modifications of model physics and parameterizations in the new generation of GCMs.

26

27 **1 Introduction**

28 Sea ice is the key feature of high-latitude climate through its role in the surface energy budget, ocean and
29 atmosphere dynamics, and marine ecosystems. Over the recent decades, the Arctic has witnessed unprecedented sea ice loss,

30 which is a key indicator of global climate change (e.g. Onarheim et al., 2018; Serreze and Meier, 2019), driven both by
31 anthropogenic activities and internal climate variability (e.g. Notz and Stroeve, 2016). Arctic sea ice has declined in every
32 month of the year with the strongest trends in September, a sea ice extent (SIE) reduction of 79000 km² yr⁻¹ in the period
33 1979-2022, compared to that in March, with -39200 km² yr⁻¹ over 1979-2022 (<http://nsidc.org/arcticseaicenews/2022/>). The
34 overall decrease in SIE reveals large seasonal and regional variability. Although winter sea ice loss is dominated by the
35 reduction in the Barents Sea (Årthun et al., 2021), the most pronounced summer sea ice decrease occurs in the East Siberian
36 Sea (that explains more than 20% of the September trend, (Watts et al., 2021) and in the Beaufort, Chukchi, Laptev and Kara
37 seas (Onarheim et al., 2018). Along with a severe reduction in sea ice coverage, Arctic sea ice has also thinned, with a ~70%
38 reduction in summer sea ice volume (SIV) ~~from over~~ 1979 ~~to~~ 2021 (<https://nsidc.org/>). As a consequence, the Arctic ice is
39 getting younger: the portion of the multi-year ice, which previously was the iconic feature of the Arctic, has decreased from
40 ~30% in 1985 (beginning of the satellite era) to ~4.4% in 2020 in winter months (Perovich et al., 2020). The Arctic transition
41 toward a first-year ice regime might substantially alter the interactions in the ocean-atmosphere-ice system (Aksenov et al.,
42 2017). The changes in total SIE and sea ice thickness (SIT) cause a redistribution of the sea ice classes, in particular the
43 marginal ice zone (MIZ) is strongly affected (Rolph et al., 2020). The Arctic MIZ has held interest as the fundamental region
44 supporting many physical, biological and biogeochemical processes (Tàpias et al., 2021). The MIZ is traditionally defined as
45 the region where polar air, ice, and water masses interact with the ocean temperature and subpolar climate system (Wadhams
46 and Deacon, 1981). It corresponds to the portion of the ice-covered ocean often characterised by highly variable ice
47 conditions, where surface gravity waves significantly impact the dynamics of sea ice (e.g. Dumont et al., 2011). Due to the
48 large uncertainties in observed and forecasted waves within sea ice, the MIZ is still operationally defined through a sea ice
49 concentration (SIC) thresholds, as the transition zone between open water and consolidated pack ice, where the total area of
50 the ocean is covered by 15-80% of sea ice (e.g. Strong, 2017; Paul et al., 2021; Rolph et al., 2020). While there are no
51 significant changes in the area of the Arctic MIZ during the satellite era (Rolph et al., 2020), the marginal ice zone fraction
52 (MIZF) defined as the percentage of total sea ice area (SIA) covered by MIZ (Horvat, 2021) increases by more than 50% in
53 August and September as the total SIA drastically decreases (Rolph et al., 2020; Horvat, 2021). Since the MIZ differs from
54 the pack ice in higher sensitivity to the dynamic and thermodynamic forces, the growing MIZF changes the Arctic response
55 to global warming, which may worsen the pace of sea ice melt and pose repercussions for local and global climate.

56 Assuming that the Arctic Ocean will continue to lose sea ice, a relevant question is how fast the Arctic will turn
57 ice-free in summer. Coupled climate models can be used in the prediction and projection of the climate system, including the
58 sea ice conditions. In the majority of simulations from CMIP6 (Eyring et al., 2016), the Arctic Ocean becomes practically
59 sea ice free (SIA < 1 million km²) in September for the first time before 2050 in all scenarios (Notz and SIMIP Community,
60 2020) or even by 2035 when selecting only the models that best represent the present Arctic sea ice state and northward
61 ocean heat transport (Docquier and Koenigk, 2021). Even using a process-based selection criterion, uncertainties in the
62 model projections are relatively large, which undermines the model's trustworthiness (Docquier and Koenigk, 2021).
63 Besides, the accurate simulation of past and present Arctic sea ice is still challenging. Although the CMIP6 multi-model

64 ensemble mean is closer to the observed sensitivity of Arctic sea ice to global warming (Notz and SIMIP Community, 2020;
65 Shu et al., 2020), there is little difference in overall model performance among CMIP3, CMIP5 and CMIP6. CMIP6 models
66 still simulate a wide spread of mean sea ice area and volume in March and September (Davy and Outten, 2020; Notz and
67 SIMIP Community, 2020; Watts et al., 2021).

68 Among the model developments and improvements needed to produce more accurate future projections, the
69 increase in horizontal spatial resolution is recognized to be a key step to enhance the representation of the complex processes
70 at high latitudes and to obtain trustworthy projections of ice variability. In order to address the impact of the model grid
71 resolution on the simulated oceanic and atmospheric phenomena, the High-Resolution Model Intercomparison Project
72 (HighResMIP; Haarsma et al., 2016) was designed within the EU Horizon 2020 PRIMAVERA project (PROcess-based
73 climate sIMulation: AdVances in high-resolution modelling and European climate Risk Assessment,
74 <https://www.primavera-h2020.eu/>). HighResMIP is one of the CMIP6-endorsed model intercomparison projects, which
75 provides a useful framework to investigate the role of the enhanced horizontal resolution in representing the features of the
76 climate system. A number of climate modelling groups contributed to the project providing the same simulations in at least
77 two different configurations. The impact of the increased resolution within the HighResMIP is examined in many studies
78 with regard to atmosphere, sea ice, and ocean components of the climate systems (e.g., Fuentes-Franco and Koenigk, 2019;
79 Docquier et al., 2019; Bador et al., 2020; Roberts et al., 2020; Jackson et al., 2020; Lohmann et al., 2021; Meccia et al.,
80 2021). ~~Even though~~ ~~Despite the fact that~~ high-resolution models can resolve specific dynamical features, the role of the
81 enhanced horizontal resolution is not uniform across ocean regions and models. Grist et al. (2018) demonstrated that refining
82 the ocean grid to eddy-permitting resolution raises the Atlantic meridional heat transport and improves the agreement with
83 observational estimates - they also show the significantly smaller impact of atmosphere resolution on the strength of the heat
84 transport. Docquier et al. (2019) confirmed this finding and showed that a better representation of Atlantic surface
85 characteristics, velocity fields, and sea surface temperature (in addition to transports toward the Arctic) improves the
86 representation of the Arctic SIA and SIV. Nevertheless, the role of ocean resolution in the representation of ocean heat
87 transport (OHT) and SIA is less clear when considering the regional effect on specific Arctic sectors, as shown for the
88 Barents Sea in Docquier et al. (2020).

89 Here, we focus on the impact of horizontal resolution on the Arctic sea ice properties in the past and future at
90 hemispheric and regional scales using the model outputs from coupled historical (hist-1950) and future (highres-future) runs
91 from HighResMIP. We assess seasonal and interannual variability and trends in the SIA and SIV, and examine when the
92 Arctic will see its first ice-free summer. We aim to explore the role of enhanced ocean/atmosphere horizontal resolution in
93 the representation of past and current sea ice and to provide some insight into whether the grid refinement improves the
94 model performance in predicting the future Arctic sea ice conditions.

95

96 2 Data

97 In this study, we analyse the outputs from the six coupled climate models participating in the HighResMIP. We use
 98 coupled runs with historical forcing (hist-1950) covering the period 1950-2014 and future projections (highres-future) from
 99 2015 to 2050 based on the Fossil-fueled development SSP5-8.5 scenario. For the ocean, five models use the Nucleus for
 100 European Modelling of the Ocean framework (NEMO, Madec et al., 2016), yet different versions, whereas MPI-ESM is
 101 based on the Max Planck Institute Ocean Model (MPIOM, Junglauss et al., 2013). The basic characteristics of the models are
 102 given in Table 1. Because each of the models uses at least two different resolutions, we evaluate 14 configurations in total.
 103 CMCC-CM2 and MPI-ESM use one ocean (eddy-permitting) resolution with two different atmospheric grids. ECMWF-IFS
 104 and EC-Earth3P run two of three configurations with an eddy-permitting ocean and different atmosphere resolutions. In
 105 other models, ocean and atmosphere resolutions vary in concert among configurations. ECMWF-IFS is not considered in the
 106 analysis of future projections since it does not provide the outputs from highres-future experiments. It is important to note
 107 that ECMWF-IFS, EC-Earth3P and CNRM benefit from several ensemble members (eight, three and six members for
 108 ECMWF LR, MR and HR, respectively; three members for both configurations of EC-Earth3P and CNRM). Given a small
 109 ensemble size of multi-ensemble configurations, a clear assessment of internal variability is not feasible in the context of this
 110 paper. We use only the first ensemble member in this study. ~~To support our choice we provide an additional analysis based
 111 on ECMWF LR and HR runs which shows the evidence that using the first individual member is not a large limitation of our
 112 study. (Supplementary).~~

113 ¶

114 **Table 1. Models and specifications of their configurations used in the study.**

Model configuration		nominal ocean resolution (°)	nominal atmosphere resolution (km)	model components	
				ocean-sea ice	atmosphere
CMCC-CM2 (Cherchi et al., 2019)	HR	0.25	100	NEMO3.6+CICE4.0	CAM4
	VHR	0.25	25		
CNRM-CM6-1 (Voldoire et al., 2019)	LR	1	250	NEMO3.6+GELATO6	ARPEGE6.3
	HR	0.25	100		
ECMWF-IFS (Roberts et al., 2018)	LR	1	50	NEMO3.4+LIM2	IFS cycle43r1
	MR	0.25	50		
	HR	0.25	25		

EC-Earth3P (Haarsma et al., 2020)	LR	1	100	NEMO3.6+LIM3	IFS cycle36r1
	HR	0.25	50		
HadGEM3 (Williams et al., 2018)	LM	1	250	NEMO3.6+CICE5.1	UM
	MM	0.25	100		
	HM	0.25	50		
MPI-ESM (Müller et al., 2018)	HR	0.4	100	MPIOM1.6.3	ECHAM6.3
	XR	0.4	50		

115

116

117

118

119

120

121

122

123

124

125

126

127

128

129

130

131

132

133

134

135

136

137

For the past sea ice properties, we mainly focus on the time period from 1979 to compare model results with available satellite records. The simulated SIA is validated against satellite observations. We use monthly SIC from two satellite-based products: the NOAA/NSIDC Climate Data Record (version 4, Meier and Stewart., 2021, hereafter CDR) and EUMETSAT OSISAF Climate Data Record and Interim Climate Data Record (release 2, products OSI-450 and OSI-430-b, Lavergne et al., 2019) both for the period 1979-2021. CDR uses gridded brightness temperatures in low frequencies from the Nimbus-7 SMMR (18, 37 GHz) and the DMSP series of SSM/I and SSMIS passive microwave radiometers (19.4, 22.2, 37 GHz). Different ratios of frequencies are used to filter weather effects. The output data are distributed on a 25 km x 25 km polar stereographic grid. CDR algorithm blends the NASA Team (NT; Cavalieri et al., 1984) and the Bootstrap (BT; Comiso, 1986) by selecting the higher concentration value for each grid cell, so taking advantage of the strengths of each algorithm to produce concentration fields that are more accurate than those from either algorithm alone (Meier, 2014). OSISAF comprises two SIC products based on passive microwave sensors: OSI-450 (from 1979 to 2015) and OSI-430-b, extension from 2016 onwards. OSI-450 uses data from the SMMR 1979-1987), SSM/I (1987-2008), SSMIS (2006-2015) instruments (19.35 and 37 GHz frequencies) together with Era Interim reanalysis (Dee et al., 2011), while OSI-430-b is based on SSMIS and operational analysis and forecast from ECMWF. We use estimates of SIT and SIV from the Pan-Arctic Ice Ocean Modeling and Assimilation System (PIOMAS; Zhang and Rothrock, 2003) that comprises the global Parallel Ocean and sea Ice Model (POIM) coupled to eight-category thickness and enthalpy distribution sea ice model and a data assimilation of SST (from NCEP/NCAR reanalysis, Kalnay et al., 1996) and SIC (from the NSIDC near-real time product; Brodzik and Stewart, 2016). PIOMAS proved its credibility against in-situ measurements (Stroeve et al., 2014; Wang et al., 2016) and therefore it is widely used in numerous intercomparison studies as the observational proxy (e.g. Labe et al., 2018). Note that PIOMAS tends to underestimate the thick ice north to Greenland and the Canadian Arctic Archipelago and overestimate SIT in the areas of thin ice (Stroeve et al., 2014; Wang et al., 2016). Monthly fields of SIC and effective SIT from 1979 to 2021 are

138 used in this work. We describe sea ice coverage in terms of SIA (the integral sum of the product of ocean grid-cell areas and
139 the corresponding sea ice concentration), instead of SIE (the integral sum of the areas of all grid cells with at least 15% of
140 SIC). To compute SIV, the equivalent SIT (the sea ice volume per grid-cell area) is multiplied by the individual grid-cell
141 area, and then summed over the Arctic region. To derive integrative metrics, only the grid cells with at least 15% SIC are
142 considered owing to the high uncertainty in passive microwave retrievals in low sea ice conditions. Apart from model
143 evaluation at the hemispheric scale, we provide a regional analysis of sea ice variability in six subregions of the Arctic Ocean
144 (north of 65°N) as defined in Figure 1.

145 **3 Results**

146 **3.1 Mean state**

147 First, we assess the spatial patterns of simulated ice properties against observational-based estimates over the
148 historical period restricted from 1979 to 2014. Figure 2 shows the climatological mean distribution of SIT in March and
149 September for model outputs and PIOMAS. The mean position of 15% and 80% SIC edges is also shown from each model
150 and CDR (over PIOMAS). In general, most models struggle to reasonably simulate the spatial pattern of SIT and produce
151 either thicker (ECMWF-IFS, EC-Earth3P, CMCC-CM2 VHR4) or thinner (CNRM-CM6, MPI-ESM) ice over a vast area
152 compared to PIOMAS. Some models are able to correctly locate the thickest ice north of Greenland and the Canadian Arctic
153 Archipelago and the thinner ice in the Siberian Shelf Seas (HadGEM3, CMCC-CM2 HR4), but the simulated ice can thicken
154 up to 7 m. EC-Earth3P HR and ECMWF-IFS MR, despite capturing the overall SIT pattern, simulate high thickness also in
155 the East Siberian and Chukchi Seas, which is clearly visible in March. This might be related to unrealistic sea ice drift. As in
156 PIOMAS, most models reproduce changes in the SIT between March and September with a more pronounced seasonal
157 retreat in the Siberian sector.

158 There is no direct effect of horizontal resolution on the spatial distribution of SIT. Increasing ocean resolution, the
159 mean SIT decreases for ECMWF-IFS, does not change notably for HadGEM3 and CNRM-CM6, and increases for
160 EC-Earth3P. The role of atmosphere resolution also depends on the model: for example, the finer atmosphere resolution
161 MPI-ESM reproduces on average slightly thinner ice compared to LR configuration, while the finer CMCC-CM2 simulates
162 thicker ice over a larger area. Biases in the representation of SIT pattern can be related to poor representation in surface
163 pressure and large-scale atmospheric patterns (Kwok and Untersteiner, 2011; Stroeve et al., 2014), sea ice motion and ocean
164 forcing (Watts et al., 2021).

165 Most models tend to realistically simulate the position of the sea ice edge both in March and September. The LR
166 configuration of ECMWF-IFS tends to overestimate the sea ice cover far south in the North Atlantic and the North Pacific
167 Oceans compared to CDR. The bias can be explained by the poor representation of the ocean advection. ~~In fact,~~ Docquir et
168 al. (2019) showed that the northward OHT is improved when ocean resolution increases from 1° to 0.25°, both across the
169 Bering Strait (83 km wide) and through the Nordic Seas establishing the Atlantic warm inflow into the Arctic Ocean.

170 Similarly, as for SIT, the effect of the atmospheric grid resolution on the sea ice extent is model-dependent. When it is
171 enhanced, there are no notable changes in the location of the March ice edge in the ECMWF-IFS and HadGEM3 models,
172 while it is largely overestimated in CMCC-CM2 and MPI-ESM, particularly in the Nordic Seas. Specifically, CMCC-CM2
173 HR4 underestimates March sea ice coverage in the northern Barents Sea, the Bering Sea, and the Sea of Okhotsk, whereas
174 the VHR4 version (with a finer atmospheric grid) reproduces a reasonable amount of winter ice in marginal seas. In
175 September, higher atmosphere resolution leads to a larger SIA in ECMWF-IFS and CMCC-CM2, conversely it has an
176 opposite effect in HadGEM3 and MPI-ESM models. In addition, MPI-ESM XR does significantly melt sea ice in the
177 Siberian seas which are almost ice-free in summer. The width of the MIZ (marked in Figure 2 by the area capped between
178 15% and 80% SIC contours) also varies among different models. In many of them, March MIZ similarly surrounds the inner
179 ice pack, comparing well with CDR. In September, most models fairly simulate an extension of MIZ comparable to the
180 observed one. Exceptions are MPI-ESM runs that lose all consolidated pack ice in summer and ECMWF LR that tends to
181 overestimate the total and pack ice, with a small portion covered by marginal ice in the Barents Sea and Nordic Seas.

182 3.2 Seasonal variability

183 Figure 3 shows the mean seasonal cycle of the total Arctic SIA and SIV computed over the 1979-2014 period.
184 Satellite estimates from both OSISAF and CDR are included to validate the models' outputs. The CDR Arctic ice area
185 expands to its maximum in March, with coverage of nearly $14 \times 10^6 \text{ km}^2$, and returns to its minimum in September at around
186 $6 \times 10^6 \text{ km}^2$. Similar seasonality is displayed by the OSISAF dataset, which has just a slightly smaller SIA in all months.
187 As in CMIP5 and CMIP6 low-resolution models (Shu et al., 2020, Notz and SIMIP Community, 2020), most HighResMIP
188 models adequately reproduce the mean seasonal cycle of SIA with the melt season starting in March and lasting until
189 September where a minimum is reached (Figure 3a). There is a considerable spread among models, it is relatively larger in
190 winter than in summer. March SIA ranges from 12 to $20 \times 10^6 \text{ km}^2$, while September values lie in the range between 3 and
191 $7.5 \times 10^6 \text{ km}^2$ in all but one model. The ECMWF-IFS LR overestimates the Arctic SIA all year round, but it can properly
192 represent the amplitude of SIA seasonal variability and hence correctly reproduces the ice advance and retreat phases. The
193 comparison between the model configurations indicates that finer resolution generally results in simulated SIA closer to
194 satellite products. The effect of changing atmosphere resolution varies among models, though. For instance, the CMCC-CM2
195 HR constantly stays in the lower bound of the model ensemble and reproduces a weaker amplitude of the seasonal cycle
196 compared to observations; applying the atmospheric grid refinement (CMCC-CM2 VHR4 configuration) favourably
197 increases sea ice coverage and does not significantly change the seasonal cycle amplitude. Different impact is observed for
198 the MPI-ESM model: the finer atmospheric grid leads to closer agreement with observations in SIA during winter but
199 increases the spring/summer melting resulting in an underestimated September minimum up to ~50% compared to
200 observations. In general, in other HighResMIP runs, the atmosphere grid refinement gives smaller changes to Arctic sea ice
201 coverage compared to the ocean resolution enhancement. In the ECMWF-IFS, the LR shows a constant SIA overestimation,
202 that is largely resolved in the model configuration with an eddy-permitting ocean (HR), particularly in summer. The same

203 behaviour is seen for six ECMWF ensemble members (Figure S1). As for the CMCC-CM2 model, a further refinement in
204 the atmosphere resolution increases the SIA in the whole year with the best agreement with observation from October to
205 July. The HadGEM3 runs are relatively close to observations in summer but they tend to overestimate the sea ice growth -
206 the impact of increased ocean and atmosphere resolution is evident for this model with a strong reduction of winter sea ice of
207 ~25% from LL to HM and a smaller but still remarkable contraction in summer. Here, the increase in the atmosphere
208 resolution further reduces SIA in contrast to previous models. Finally, EC-Earth3P and CNRM-CM6 models show negligible
209 differences between model configurations, despite ocean and atmosphere grids resolution.

210 In our reference product, PIOMAS, the Arctic SIV ranges from $\sim 25 \times 10^3 \text{ km}^3$ at its peak in April to $\sim 10 \times 10^3 \text{ km}^3$ at
211 its minimum in August/September (Figure 3b). All models capture the timing of the SIV maximum in April and the
212 minimum in August/September with a realistic seasonal cycle amplitude that ranges between 15 and $20 \times 10^3 \text{ km}^3$. However,
213 there is a large spread among different models, with most models overestimating PIOMAS - ECMWF-ISF LR is a clear
214 “outlier” exceeding $70 \times 10^3 \text{ km}^3$ in April and $50 \times 10^3 \text{ km}^3$ in September. Although in some models the bias in SIA is
215 seasonally dependent with larger errors in winter, bias in simulated SIV is consistent throughout the year in all models. In
216 general, large SIV is mainly due to poorly simulated SIT rather than incorrect sea ice cover (Figure 2, 3a). Only in
217 ECMWF-IFS LR, the combination of large ice expansion and extremely thick ice leads to unrealistically high SIV. The SIV
218 overestimation in the CMCC-CM2 and EC-Earth3P models is caused by too thick sea ice, even though their SIA compare
219 well with observations. Only one model (CNRM-CM6 in both configurations) has thin ice and hence low bias in SIV
220 compared to PIOMAS, all year round. The changes in resolution have no visible impact in this case. The increase of only
221 ocean resolution largely improves the representation of SIV (as for SIA) in ECMWF-IFS with a large volume reduction
222 (including six ensemble members; Figure S1), but does not affect the volume seasonality in HadGEM3. Finer atmosphere
223 resolution and the combined resolution increase tend to increase the ice volume except in HadGEM3 and MPI-ESM.
224 MPI-ESM has a good fit to PIOMAS for SIV although this model underestimates SIA and cannot simulate consolidated pack
225 ice (SIC > 80%, Figure 2).

226 In addition to the total SIA, we show the seasonal variability of the area covered by marginal ice over the same
227 1979-2014 period (Figure 4a). It is worth noting that the evaluation of the simulated MIZ area is highly dependent on the
228 reference product used, particularly in summer. This can be mainly ascribed to the treatment of the wet surface (e.g. melt
229 ponds, snow wetness) that poses difficulty to retrieve the SIC using passive microwave radiometers (Ivanova et al., 2015).
230 OSISAF has a small portion of MIZ in winter, while it overestimates CDR from May to November. The maximum difference
231 between the two products is up to nearly $0.9 \times 10^6 \text{ km}^2$ in July. The observed MIZ seasonal variability contrasts with that
232 shown by the total ice area: the MIZ expands in spring, when the consolidated pack ice starts to melt, and this process leads
233 to the MIZ area peak occurring in summer. After reaching its maximum in July, the marginal ice starts to melt and its area
234 decreases until September, simultaneously with the total and the consolidated pack ice cover. Before the next year's melting
235 season, the MIZ stays relatively stable but with a secondary peak in October, at the beginning of sea ice advance. The models
236 are overall able to simulate the seasonal cycle, reasonably capturing the phases of the MIZ expansion and retreat. However,

237 they tend to overestimate the MIZ in winter, but most of them ~~lie~~ are lying between the OSISAF and CDR summer estimates.
238 Generally, models struggle to properly simulate the timing and magnitude of the MIZ maximum: ECMWF-IFS LR is higher
239 than observations from November to May due to a large overestimation of the total ice area, nevertheless it lies between
240 CDR and OSISAF in the rest of the year. Noteworthy, the ECMWF-IFS finer resolution configurations are in better
241 agreement with observed values. In the HadGEM3 LL configuration, the marginal ice expansion starts earlier, with a large
242 bias of the MIZ area from March to June. Increasing resolution in HadGEM3 model does not have a visible impact for the
243 rest of the year. The impact of changes in the ocean and atmosphere resolution is small for other models. Finally, MPI-ESM
244 configurations fail to reproduce the MIZ seasonal cycle from June to November. This pairs with Figure 2, which shows
245 underestimation of consolidated pack ice and MIZ predominance in the MPI-ESM runs.

246 We also show the seasonal cycle of the MIZ area fraction (MIZF) from 1979 to 2014, calculated from the model
247 and satellite products outputs (Figure 4b). The MIZF is defined as the percentage of the ice cover that is MIZ (Horvat, 2021)
248 and reflects the relative changes of the MIZ, which are highlighted since the total ice experiences substantial seasonal
249 variability. The observed MIZF ranges from 5-10% in winter to 20-40% at its maximum between June/July. For all models,
250 the simulated MIZF maxima are delayed compared to the satellite estimates and ~~to~~ the MIZ area by about one month, when
251 the total ice area approaches the September minimum and the MIZ area is still large. ~~Notably, it is notable that~~
252 HighResMIP models are in better agreement with observations when considering the MIZF rather than the MIZ area.
253 Excluding the MPI-ESM configurations, all models are in general agreement from November to May; the model spread
254 enlarges in spring/summer but the models lie anyway within the observation envelope. The use of the MIZF metric
255 highlights the peculiar representation of Arctic sea ice in the MPI-ESM: up to 95% of sea ice in the model consists of
256 marginal ice.

257 3.3 Seasonal variability in the sub-regions

258 Since sea ice changes in the Arctic region are not uniform in space and time as a result of local climate effects (cf.
259 Parkinson et al 1999; Meier et al 2007, Peng and Meier 2018), it is important to monitor the sea ice change also on regional
260 scales. We analyse the seasonal variability of SIA and SIV in six sub-regions and we compare it with that of reference
261 products (Figure 5, Table 2).

262 Satellite estimates of SIA are not shown in the Central Arctic sector (CA) due to the observation gap near the North
263 Pole. In this region, all models simulate a pronounced seasonal cycle in SIA with the widest area between December and
264 April, and a minimum in August. Although ~~most~~ the majority of the models agree in winter when the region is fully covered
265 by sea ice, the inter-model spread increases in summer. HadGEM3 and CMCC-CM2 simulate similar seasonal cycles in all
266 configurations with slightly lower values in HadGEM3 HM. The ECMWF-IFS LR is an outlier also in this region, with a
267 large SIA all year round and a minimum in August that is as large as the autumn/winter values in other models. Also
268 EC-Earth3P LR has SIA comparable to ECMWF-IFS LR from November to May, however it overestimates the melting and
269 growing phases with an August minimum comparable to other models. The CNRM-CM6 model produces the smallest

270 seasonal cycle amplitude in both resolutions, with a decrease between the winter values and the minimum of ~10%. On the
271 contrary, both MPI-ESM configurations display the strongest seasonal cycle, with the largest area in winter and the smallest
272 in summer. These differences among models do not clearly depend on the resolution changes. For SIV, PIOMAS shows an
273 increase of ~30% between the minimum in August/September and the maximum in May. The seasonal cycle magnitude is
274 captured by most models but with a large spread mainly driven by differences in the simulated thickness (Figure 2). The
275 models generally perform similarly in simulating the SIV seasonal cycle in the sub-regions as at the hemispheric scale
276 (Figure 3b). For the sake of conciseness, only the specific features of the SIV representation at the regional scale will be
277 indicated below. The Barents-Kara Seas (B-K) is the only sub-region where satellite products show a distinct maximum peak
278 that occurs in April (one month ~~after~~ later the hemispheric SIA maximum), cf. Figure 5a. Except for CMCC-CM2, the
279 models generally overestimate SIA in winter with a large spread among them which reduces in summer, when models are in
280 closer agreement with satellite estimates. The strong underestimation of SIA in the CMCC-CM2 HR4 configuration could be
281 attributed to the increased poleward Atlantic OHT simulated by this model (Docquier et al., 2020). The warmer ocean
282 temperatures not only promote sea ice melting in winter but also hinder its growth in autumn. The ocean and atmosphere
283 spatial resolution have generally the opposite effects on simulated SIA. Increasing only the ocean resolution in ECMWF-IFS
284 (from LR to MR) and HadGEM3 (from LL to MM) results in lower SIA and a better fit to the observations. Conversely,
285 increasing the atmosphere resolution generally leads to larger SIA, except for a decrease in SIA for HadGEM3. The
286 combined effect of enhanced resolution in both ocean and atmosphere in CNRM-CM6 and EC-Earth3P models increases the
287 winter SIA, worsening the comparison with the observations. For SIV, nearly a half of the model ensemble is within the 15%
288 of PIOMAS seasonal variability from January to June which is not the case for other sectors. The Barents-Kara Seas is the
289 only region where CMCC-CM2 HR underestimates SIV as a result of too low SIA. In addition, both configurations of
290 CMCC-CM2 underestimate the seasonal variation of SIV. At the same time, CNRM-CM6 has a better fit to PIOMAS SIV
291 in the Barents-Kara Sea sector compared to the other parts of the Arctic Ocean. The increased ocean resolution has a clear
292 positive effect on SIV representation in ECMWF-IFS configurations, whereas other models display similar values when
293 changing such parameter. On the other hand, the enhanced atmosphere resolution leads to higher SIV for ECMWF-IFS and
294 CMCC-CM2, lower SIV for HadGEM3 and does not affect SIV in MPI-ESM.

295 The Laptev (LV), East Siberian (ESS), and Beaufort-Chukchi Seas (B-C) show similar behaviour in SIA and SIV.
296 They can be analysed together and grouped as in Peng and Meier (2018). In these regions, there is no noticeable peak in the
297 observed seasonal variability of SIA, instead the annual maximum is extended between December and May since the winter
298 sea ice expansion is constrained by land. In spring, the downward shortwave radiation increases, causing the rapid sea ice
299 melt, which ends in September. Notably, the disagreement between satellite estimates in summer SIA is higher in all three
300 regions probably due to the enhanced presence of melt ponds, which complicate the SIC retrievals from passive microwave
301 radiometers (Ivanova et al., 2015). The models exhibit better agreement in winter, while the spread across models is larger in
302 summer. This could be possibly associated with the model differences in simulating atmospheric circulation, as well as the
303 river discharge (Park et al., 2020) and the transport of Pacific waters through the Bering Strait (Watts et al., 2021), which

304 modify the thermo-haline structure of the upper-ocean and affect sea ice growth and melt. In all three regions, SIA from
305 ECMWF-IFS LR is well compared with satellite estimates in winter, which is not the case for other sectors with a greater
306 role of the Atlantic OHT where the model is biased high. HadGEM3 overestimates SIA, particularly in its lower resolution
307 configuration. This behaviour is common also for other parts of the Arctic Ocean which points out that bias in HadGEM3 is
308 similarly distributed across the regions. MPI-ESM underestimates SIA ~~to~~with a greater degree in summer since the model is
309 struggling to simulate consolidated pack ice (Figure 2). CNRM-CM6, CMCC-CM2 and HR of EC-Earth3P show a fairly
310 good agreement with satellite estimates in all three regions. Lower resolution configuration of EC-Earth3P displays an earlier
311 and faster sea ice retreat in the Laptev and East Siberian Seas resulting in the second-lowest SIA, while the model compares
312 well with OSISAF estimates in the Beaufort-Chukchi Seas. Increased ocean resolution leads to lower SIA for all models
313 except for EC-Earth3P which has higher values in its HR configuration. The effect of the ocean resolution is stronger in
314 summer, however the impact is substantial all year round for HadGEM3. Enhancement of the atmosphere resolution does not
315 significantly affect ECMWF-IFS but leads to higher summer SIA in CMCC-CM2, as in the other regions. For MPI-ESM, the
316 increase in atmosphere resolution has a larger impact on summer SIA in the Laptev, East Siberian, and Beaufort-Chukchi
317 Seas compared to other sectors: MPI-ESM XR simulates SIA almost twice lower than CDR in August and September. In the
318 Laptev, East Siberian, and Beaufort-Chukchi Seas, SIV reaches the maximum in May (April-May in B-C) while the annual
319 minimum occurs in September. Most models overestimate SIV with the highest bias (ECMWF LR) in the East Siberian and
320 Beaufort-Chukchi Seas. CMCC-CM2 HR and MPI-ESM HR are the closest to PIOMAS, even though the latter fails to
321 reasonably simulate the SIC (Figure 2). The effect of the ocean resolution on SIV is clearly seen for ECMWF-IFS and
322 EC-Earth3P in all three regions and for HadGEM3 in the Laptev Sea - the only region where LL and MM configurations of
323 HadGEM3 differ. Other models do not show considerable differences in SIV when changing ocean resolution. Finally,
324 increased atmosphere resolution results in higher SIV for ECMWF-IFS, EC-Earth3P, and CMCC-CM2 and lower SIV for
325 HadGEM3 and MPI-ESM.

326 The Greenland region (GD) holds the largest area of sea ice both in winter and summer (3 and 1.5×10^6 km²
327 respectively according to the satellite estimates). Most models tend to overestimate SIA all year round with the highest bias
328 in winter in ECMWF-IFS LR and HadGEM3. The models are generally capable of melting away the excess of sea ice by
329 August, so there is more consistency among most models in summer, when MPI-ESM underestimates SIA more than all of
330 them. An increase in the ocean resolution from 1° to 0.25° effectively improves the representation of SIA in ECMWF-IFS,
331 whereas it does not give notable changes in HadGEM3 and EC-Earth3P. The effect of atmosphere resolution again depends
332 on the model. ECMWF-IFS and CMCC-CM2 display slightly higher SIA in their finer atmosphere configurations,
333 particularly in winter. Conversely, HadGEM3 has lower SIA in its HM configuration in winter, which fits better to the
334 observations. For MPI-ESM, there are no differences between different configurations, as in the Barents-Kara Seas region.
335 For SIV, both configurations of CMCC-CM2 have a large error in the Greenland region owing to high bias in SIT (Figure 2);
336 whilst at least one configuration of the model is in good agreement with PIOMAS in other sectors. Enhanced ocean
337 resolution leads to lower SIV for ECMWF-IFS and higher SIV for EC-Earth3P. At the same time, there are no significant

338 differences between configurations of HadGEM3 and CNRM-CM6 with changing ocean resolution. An increase in the
339 atmosphere resolution has almost no effect on SIV in HadGEM3 and MPI-ESM but leads to higher SIV in CMCC-CM2
340 The displayed analysis reveals that the model performance and the accuracy of simulated SIA largely depend on the
341 Arctic region and the season studied. While the Barents-Kara Seas and Greenland regions contribute mainly to the winter
342 inter-model spread, the largest summer differences among models are seen in the Laptev, East Siberian and
343 Beaufort-Chukchi Seas. There are no considerable differences in the model ability to simulate SIV at the regional scale, in
344 fact the biases are generally uniform across regions and seasons. Generally, we find no strong dependence of sea ice realism
345 from the horizontal resolution. The impact of the ocean resolution on the representation of SIA is most pronounced in the
346 Barents-Kara Seas and Greenland sea ice regions that are strongly influenced by the Atlantic OHT. The effect of the
347 atmosphere resolution is less clear but there is evidence that the atmosphere resolution has a stronger impact on SIV rather
348 than on SIA and particularly in the regions of thicker ice (B-C, GD).

349

350 Table 2. March and September SIA for each region (except CA) in each model for 1979-2014.

	March (10^6 km 2)					September (10^6 km 2)				
	BK	LV	ESS	B-C	GD	BK	LV	ESS	B-C	GD
ECMWF-IFR LR	3.06	1.1	1.57	2.16	4.05	1.87	0.84	1.41	1.73	3
ECMWF-IFR MR	2.12	1.08	1.56	2.15	3.22	0.62	0.57	1.19	1.56	1.45
ECMWF-IFR HR	2.46	1.09	1.56	2.14	3.53	1.06	0.64	1.25	1.61	1.7
EC-Earth3P	2.13	1.11	1.58	2.18	3.17	0.45	0.35	0.74	1.26	1.56
EC-Earth3P HR	2.43	1.1	1.57	2.17	3.32	0.72	0.52	1.06	1.56	1.43
CNRM	2.39	1.11	1.58	2.19	3.43	0.76	0.66	0.68	1.12	1.26
CNRM HR	2.64	1.1	1.57	2.17	3.35	0.6	0.47	0.8	1.2	1.08
HadGEM3 LR	2.89	1.31	1.85	2.31	4.29	0.78	0.71	1.22	1.45	1.8
HadGEM3 MM	2.7	1.23	1.68	2.3	4.41	0.79	0.6	1.17	1.59	1.68
HadGEM3 HM	2.38	1.17	1.63	2.24	3.84	0.4	0.43	0.95	1.46	1.45
CMCC-CM2	1.4	1.1	1.56	2.13	2.9	0.22	0.47	0.68	1.05	1.41

HR										
CMCC-CM2 VHR	1.98	1.11	1.57	2.15	3.25	0.66	0.63	1	1.44	1.76
MPI-ESM HR	2.31	1.03	1.52	2.1	2.93	0.42	0.38	0.68	0.95	0.72
MPI-ESM XR	2.48	1.04	1.53	2.11	3.39	0.37	0.24	0.36	0.62	0.65
CDR	2.19	1.11	1.58	2.18	3.07	0.64	0.54	0.9	1.28	1.38
OSISAF	2.09	1.11	1.57	2.15	2.97	0.56	0.48	0.8	1.17	1.28

351

352 3.4 Interannual variability and trends

353 Next, we evaluate the long-term variability of the Arctic SIA and SIV from the hist-1950 simulations from 1979 to
354 2014. Figure 6a illustrates monthly anomalies of SIA (with respect to 1979-2014 climatologies) simulated by the models and
355 derived from satellite data sets. The inter-model spread is relatively similar throughout the period but it increases from the
356 mid-2000s when the ice reduction has accelerated. All models are able to reproduce the sea ice shrinking but with varying
357 intensity: ECMWF-IFS LR, HadGEM3 LL, MPI-ESM HR show larger negative trends compared to observations (-44×10^3
358 $\text{km}^2 \text{yr}^{-1}$ in CDR and $-46 \times 10^3 \text{km}^2 \text{yr}^{-1}$ in OSISAF), while the MR and HR versions of ECMWF-IFS, both configurations of
359 CNRM-CM6, EC-Earth3P, HadGEM3 HM, and CMCC-CM2 HR display weaker negative trends (Table 3). An increase in
360 the ocean resolution generally results in smaller negative trends except for EC-Earth3P which shows a similar decline rate in
361 both configurations. Note that ~~the~~ weaker trends are also observed in six HR ensemble members of ECMWF-IFR in
362 comparison to their low-resolution counterparts (Table S1). The effect of finer atmosphere resolution is different among
363 models: the SIA decrease is stronger in ECMWF-IFS and CMCC-CM2 and weaker in HadGEM3 and MPI-ESM.

364 Figure 6b shows monthly anomalies of SIV (with the seasonal cycle removed) over 1979-2014 in HighResMIP
365 models and PIOMAS. There is a substantial inter-model spread for SIV compared to SIA, particularly at the beginning and
366 the end of the observed period (55-85% of yearly averaged SIV from PIOMAS). The biases from a few models are not
367 consistent throughout the years varying significantly from positive to negative (EC Earth-3P HR, ECMWF MR, HadGEM3
368 LL).

369 PIOMAS simulates sea ice shrinking at the rate of $-291 \text{ km}^3 \text{yr}^{-1}$; similarly, all models simulate a SIV decrease.
370 There is no straightforward impact of changing resolution in the ocean and atmosphere on the linear trends in SIV since the
371 impact of horizontal resolution on SIA and SIT differs from with the models. However, we find that configurations with
372 coarse ocean resolution generally tend to simulate more negative trends ($-424 \text{ km}^3 \text{yr}^{-1}$ in ECMWF LR compared to -105 and
373 $-157 \text{ km}^3 \text{yr}^{-1}$ in its finer configurations; for HadGEM3, the trend ranges from $-355 \text{ km}^3 \text{yr}^{-1}$ in lower resolution to -257 and
374 $-174 \text{ km}^3 \text{yr}^{-1}$ in finer resolution configurations). We observe the same for the ECMWF ensemble members (Table S1). Here,
375 the exception is EC-Earth3P in which the eddy-permitting configuration has a larger negative trend in SIV (-322 and -460

376 $\text{km}^3 \text{yr}^{-1}$). This might be attributed to the thicker ice simulated in the HR configuration (Figure 2). In CNRM-CM6, the SIV
377 decrease is very weak (-62 and $-36 \text{ km}^3 \text{yr}^{-1}$ for LR and HR configurations, respectively), which might reflect the negative
378 ice growth-ice thickness feedback: thin ice allows sea ice to grow more rapidly mitigating the ice loss. The finer atmosphere
379 resolution has a different impact on the pace of sea ice retreat in different models: CMCC-CM2, VHR4 and ECMWF-IFS
380 HR simulate slightly stronger trends compared to their coarser counterparts ($-384 \text{ km}^3 \text{yr}^{-1}$ and $-411 \text{ km}^3 \text{yr}^{-1}$ in CMCC-CM2;
381 -105 and $-158 \text{ km}^3 \text{yr}^{-1}$ in ECMWF-IFS). On the other hand, in MPI-ESM and HadGEM3, the finer configuration has less
382 negative trend compared to the coarser one ($-337 \text{ km}^3 \text{yr}^{-1}$ and $-144 \text{ km}^3 \text{yr}^{-1}$ in MPI-ESM; -174 and $-257 \text{ km}^3 \text{yr}^{-1}$ in
383 HadGEM3).

384 We also examine how the models simulate sea ice response to the external forcing on a seasonal scale. The monthly
385 trends in the Arctic-wide SIA (computed over the period 1979-2014) reveal that the models tend to underestimate the rate of
386 sea ice loss in the melting season and in summer (not shown). Most models reproduce more negative trends from November
387 to May and underestimate the magnitude of trends in other seasons. MPI-ESM HR trends are found to have a closer fit to the
388 observed trends for the total Arctic although the model is wrong in simulating SIC and sea ice classes. For SIV, the models
389 vary greatly in the representation of trends. Despite all models being able to simulate a SIV decline in all months, they
390 cannot capture the observed magnitude of sea ice loss and have values ranging from almost 0 to $-450 \text{ km}^3 \text{yr}^{-1}$. They also
391 struggle to reproduce the seasonal cycle in the trend which in PIOMAS has a slightly stronger signal in June and a weaker
392 signal in the winter months ($-320 \text{ km}^3 \text{yr}^{-1}$ and $-260 \text{ km}^3 \text{yr}^{-1}$ respectively).

393

394 **Table 3. Linear trend in SIA and SIV and their standard deviations for 1979-2014 and 2015-2050 periods.**

	1979-2014 SIA trend ($10^3 \text{ km}^2/\text{yr}$)	2015-2050 SIA trend ($10^3 \text{ km}^2/\text{yr}$)	1979-2014 SIV trend (km^3/yr)	2015-2050 SIV trend (km^3/yr)
ECMWF-IFR LR	-72.08 ± 16.9	No future runs	-423.86 ± 68.3	No future runs
ECMWF-IFR MR	-21.24 ± 9.8		-104.82 ± 71.4	
ECMWF-IFR HR	-36.67 ± 7.6		-157.58 ± 34.4	
EC-Earth3P	-34.2 ± 9.47	-52.31 ± 16.1	-322.28 ± 31.8	-210.56 ± 64.1
EC-Earth3P HR	-40.13 ± 8.8	-54.87 ± 5.5	-460.47 ± 97.5	-368.47 ± 31.7
CNRM	-29.83 ± 8.9	-6.55 ± 13.4	-61.89 ± 23.6	-35.55 ± 26.7
CNRM HR	-15.94 ± 7.9	-63.9 ± 9.2	-35.58 ± 15.9	-131.21 ± 20.5
HadGEM3 LR	-56.54 ± 13.1	-113.91 ± 12.5	-354.64 ± 66.2	-361.87 ± 31.7
HadGEM3 MM	-48.32 ± 10.8	-97.68 ± 11.3	-256.75 ± 41.2	-459.86 ± 36.7

HadGEM3 HM	-31.54 ± 8.3	-106.72 ± 10.2	-173.72 ± 38.5	-440.09 ± 52.6
CMCC-CM2 HR	-38.57 ± 5.2	-47.55 ± 9.7	-384.2 ± 30.9	-286.38 ± 31.2
CMCC-CM2 VHR	-40.83 ± 6.6	-73.97 ± 6.6	-411.1 ± 51.1	-698.79 ± 37.5
MPI-ESM HR	-52.19 ± 5.1	-49.94 ± 8.3	-336.95 ± 22.8	-116.95 ± 19.7
MPI-ESM XR	-36.94 ± 9.5	-46.95 ± 8.5	-143.97 ± 44.5	-99.39 ± 16.4
CDR	-44.14 ± 7.3			
OSISAF	-46.42 ± 6.7			
PIOMAS			-291.27 ± 36.8	

395

396

397 Since there is a substantial difference in the models' performance in reproducing the seasonal variability on a
398 regional scale, we analyse monthly trends in SIA and SIV in each sea ice zone over 1979-2014 (Figure 7). The magnitude
399 and timing of sea ice loss strongly depend on season and region. According to observations, the winter decrease in SIA is
400 most dramatic in the Barents-Kara Seas (nearly $-17 \times 10^3 \text{ km}^2 \text{ yr}^{-1}$; $0.8\% \text{ yr}^{-1}$) while the summer trends are dominated by the
401 Eastern Siberian Sea and Beaufort, and Chukchi Seas (almost $-25 \times 10^3 \text{ km}^2 \text{ yr}^{-1}$; $2\text{-}3\% \text{ yr}^{-1}$). The Barents-Kara Seas and the
402 Greenland region show a pattern of SIA trends that differs from the total Arctic and the rest of the regions which have one
403 pronounced negative peak in September and trends close to zero in winter. Instead, in the Atlantic sector, i.e. Barents-Kara
404 seas and Greenland coast, sea ice loss is observed all year round with a slightly stronger decrease in July. In the Central
405 Arctic, the models simulate a weak SIA reduction with the strongest signal in August-September, which is not significant in
406 most models (less than 5% of the SIA of the sector). In the other sectors, the models generally tend to underestimate the pace
407 of sea ice loss indicated by satellite estimates. The exception is the Barents-Kara Seas and Greenland where some models
408 produce more negative trends compared to the observations. In the Laptev, East Siberian, and Beaufort and Chukchi Seas
409 some of the models do not simulate a reduction in summer SIA and even display weak positive trends, yet insignificant.
410 Given that all these regions hold a large MIZF in summer (Figure 4), the inability to capture trends points to inaccurate
411 sensitivity of sea ice to the external forcing, particularly within the MIZ.

412 The strongest negative trends in SIV are observed in the areas of thick ice: the Beaufort and Chukchi Seas (up to
413 $-90 \text{ km}^3 \text{ yr}^{-1}$ in September), the Greenland sector ($-80 \text{ km}^3 \text{ yr}^{-1}$ in July), and the East Siberian Sea ($-70 \text{ km}^3 \text{ yr}^{-1}$ in summer
414 months). The seasonal cycle of the Barents-Kara Sea SIV trend contrasts with those of other sectors where the highest rate of
415 sea ice decline is observed in September. Notably, in the Laptev, East Siberian, and Beaufort and Chukchi Seas, SIV
416 experiences a substantial decrease in the winter months while SIA stays nearly stable reflecting a considerable ice thinning
417 primarily driven by basal melting. In the East Siberian Sea and Beaufort-Chukchi Seas, almost all models tend to
418 underestimate trends in SIV (10 out of 14 model simulations produce less negative trends) while in the rest of the Arctic

419 zones, PIOMAS is nearly in the middle of inter-model spread. Compared to other models, both CNRM-CM6 configurations
420 and the two finest configurations of ECMWF-IFS have the changes in SIA and SIV closer to zero in almost all regions and
421 months. On the one hand, CNRM-CM6 simulates very thin ice so the lack of trend is consistent with the concept of negative
422 ice thickness-ice growth feedback. On the other hand, ECMWF-IFS MR and HR underestimate sea ice reduction everywhere
423 despite simulating very thick ice. HadGEM3 performs differently at regional scale but at least one of the configurations has a
424 very good fit to the PIOMAS estimates. Generally, both configurations of CMCC-CM2 present the large SIV decrease in all
425 sectors except for the Barents-Kara Sea and the rate of decline is similar between two resolutions despite a significant
426 difference in the mean SIV. The HR configuration of MPI-ESM is in a fairly good agreement with PIOMAS in all regions
427 except the Central Arctic and the Laptev Sea where it tends to produce more negative trends. Conversely, MPI-ESM XR
428 underestimates negative SIV trends in all parts of the Arctic Ocean except the Greenland zone where it is close to its HR
429 configuration.

430 Overall, there is no consistent link between the strength of sea ice retreat and the ocean/atmosphere resolution, it
431 rather depends on the region and the model used. Considering only SIA, the models generally underestimate the trends
432 especially in finer ocean configurations and in Laptev, East Siberian and Beaufort and Chukchi Seas in summer. However,
433 beneficial effects of increased ocean resolution for SIA trends are observed for ECMWF-IFS in the Barents-Kara Seas and
434 the Greenland area. In these regions, other models do not considerably differ between configurations; low and high-
435 resolution configurations show closer fit to the observations according to the season. Moreover, the increased atmosphere
436 resolution also does not improve the representation of SIA trends; HadGEM3, CMCC-CM2 and MPI-ESM finer atmosphere
437 configurations lead to underestimating the negative SIA trends more than their counterparts at coarse resolution. The
438 relation between ocean/atmosphere resolution and SIV trends is less clear and depends on the region and the model.

439 3.5 Future projections

440 In this section, we analyse the results of HighResMIP models when simulating future Arctic sea ice changes using
441 highres-future model outputs from 2015 up to 2050. HighResMIP future projections generally show a stronger sea ice loss
442 compared to historical runs (Table 3). These simulations can elucidate when the Arctic will reach its first "ice-free" summer,
443 i.e. the condition typically defined as the timing when September sea ice drops below 10^6 km². Reaching ice-free conditions
444 is an unprecedented change in the Arctic environment and the tipping-point in the Earth's climate system. Considering the
445 large inter-model spread in simulating observed mean sea ice state and trends, we assume that a selection of the models
446 which better agree with observations can reduce the spread and decrease uncertainty in the model projections. We select
447 models based on their historical performance of September SIA and SIV mean state and trends against CDR and PIOMAS,
448 respectively (Figure 8). To exclude outliers, we define the 75th percentile threshold and we select the models whose values
449 do not exceed the threshold for both variables. The resulting subset includes four models: low-resolution configuration of
450 EC-Earth3P, HadGEM3 MM and HM, and CMCC-CM2 HR. These models are used in the further analysis on sea ice future
451 evolution.

452 Figure 9 illustrates the September SIV time series from 1950 to 2050 computed for total Arctic and sub-regions.
453 The vertical lines mark first ice-free September in the multi-model mean with and without model selection (yellow and
454 green, respectively) and in CDR (black, data available between 1971-2021). At the regional scale, the timing of ice-free
455 conditions refers to the threshold of 25% of the CDR SIA averaged over the 1980-2010 period in the given region. It is
456 evident that huge sea ice reduction takes place in all Arctic sectors, however the pace of sea ice loss varies across the regions
457 owing to differences in the initial state and dominant processes driving the change. We can note that applying model
458 selection results in earlier timing of the ice-free conditions in Barents-Kara, Laptev, East Siberian, and Beaufort-Chukchi
459 Seas and in ice-free conditions in the total Arctic, Central Arctic, and Greenland region. In latter sub-regions, multi-model
460 mean without model selection does not predict the event everywhere before 2050. The comparison between the model
461 configurations in simulating timing of ice-free conditions shows that there is no clear link between the model resolution and
462 the pace of sea ice loss (not shown).

463 The September Arctic-wide sea ice from the multi-model mean (with model selection) shrinks by 95% from 1950 to 2050,
464 cf. top panel of Figure 9. The inter-model spread decreases throughout the century from 14×10^3 in 1950 to 1.64×10^3 km³ in
465 2050. The Arctic does not reach the ice-free conditions within 2050 in the multi-model mean without model selection,
466 although applying selection criteria advances the timing of the event up to 2047. The Central Arctic September sea ice ~~will~~
467 ~~lose~~loses 96% of its volume by 2050 in the multi-model ensemble, which is in good agreement with PIOMAS in the
468 overlapping period. The inter-model spread again narrows substantially from 2.58×10^3 km³ in 1950 to 0.23×10^3 km³ in 2050.
469 The ice-free conditions in the Central Arctic are not reached before 2050 in the multi-model mean when considering all
470 models. However, outliers' exclusion leads to approaching the threshold in 2042. The Barents-Kara Seas experiences the
471 most dramatic sea ice loss accounting for almost 100% of SIV from 1950 to 2050 in the models' ensemble. ~~The first~~
472 ice-free September in the Barents-Kara Seas is accurately simulated by the multi-model mean with model selection: the
473 event occurs in 2012 as for CDR. Avoiding model selection postpones the event by 19 years. In the Barents-Kara Seas, the
474 spread among models is decreasing from 1.46×10^3 km³ in 1950 to almost vanishing in 2050. The multi-model mean SIV in
475 the Laptev Sea shrinks by 99% during 100 years. The inter-model spread narrows from nearly 0.9×10^3 km³ at the beginning
476 of the run to 0.05×10^3 km³ in the end. The timing of the first ice-free summer is similar to that in the Barents-Kara Seas: SIA
477 drops below the threshold in 2012 for CDR and in 2032 for the multi-model mean without model selection. When applying
478 selection criteria, the ice-free conditions are reached in 2023. In the East Siberian Sea, September ensemble-mean SIV is
479 reduced by 99% by the middle of this century. The East Siberian Sea reaches the threshold in SIA earlier compared to the
480 other regions. CDR produces the event in 2007, when the Arctic broke the first record low while the multi-model mean with
481 model selection simulates ~~the~~ first ice-free conditions in 2033 (2034 without model selection). The inter-model spread ranges
482 between 4.76×10^3 km³ in 1950 and 0.1×10^3 km³ in 2050. The Beaufort-Chukchi Seas lose nearly 96% of SIV in 100 years in
483 the ensemble ~~-~~mean. The inter-model spread decreases from 3.44×10^3 km³ at the beginning to 0.37×10^3 km³ at the end of the
484 run. The multi-model mean reaches the first ice-free September in 2046. When adopting the model selection, the
485 Beaufort-Chukchi Seas ~~will bear~~ ice-free in 2039. The Greenland region is undergoing the least prominent sea ice loss

486 accounting for 88% throughout the period from 1950 to 2050. However, there is a great narrowing of the inter-model spread
487 from $6.12 \times 10^3 \text{ km}^3$ in the middle of the last century to $1.15 \times 10^3 \text{ km}^3$ 100 years after. Both multi-model means project that
488 Greenland SIA might turn ice-free in 2048. Overall, the models simulate the first ice-free September later than CDR in all
489 sub-regions studied. Therefore, we can fairly assume the same behaviour for the Total Arctic

490 Along with overall sea ice loss, there are substantial changes in the structure of sea ice cover. Figure 10 shows the
491 time series of September SIA and the MIZF from 1950 to 2050. For SIA (top panel), the models are in fairly good agreement
492 with the observations, yet have systematic biases and underestimate the negative trend. In addition, the inter-model spread is
493 large but relatively similar throughout the years ($\sim 4 \times 10^6 \text{ km}^2$). For the MIZF (bottom panel), the spread among models
494 increases considerably with time from $\sim 10\%$ in 1950 to $\sim 75\%$ in 2050. Most models simulate the MIZF growth, which
495 reflects the transition of the sea ice state to the marginal ice-dominated. The MIZ in the 2040s is projected to account for up
496 to 80% of the total ice area in September, although the interannual variability at the end of the run is large in most models.
497 CNRM-CM6 and MPI-ESM models are two outliers: CNRM-CM6 has a nearly constant MIZ fraction during the whole
498 period, while MPI-ESM has MIZF close to 100% from the beginning of the run but it occasionally drops to 0 at the end of
499 the run. Distinct models' performances in simulating MIZF show that an accurate representation of the total SIA does not
500 guarantee the same for all sea ice classes, highlighting the importance of studying the Arctic MIZ.

501 **4 Discussion**

502 Although the latest generation of the models does a fairly reasonable job in simulating the mean state and long-term
503 variability of sea ice cover (Notz and Community, 2020), the models still suffer from biases, which decrease the model's
504 trustworthiness in projecting the future sea ice state in the Arctic. The enhancement in the model components' horizontal
505 resolution is used in the CMIP6 HighResMIP as one of the factors capable of improving the realism of the model simulations
506 and reducing biases in polar regions. In this study, we investigated the ability of HighResMIP in simulating Arctic sea ice
507 variability and the impact of the ocean and atmosphere horizontal resolution on the representation of sea ice properties in the
508 recent past and future climate. We do not find a strong link between ocean/atmosphere resolution and the representation of
509 sea ice properties, and the realism of model performance rather depends on the model used. Nevertheless, there is evidence
510 that an enhanced ocean resolution leads to an improved representation of winter SIA in some models. This is associated with
511 a more accurate meridional heat transport (Docquier et al., 2019) which is a key process that can regulate the location of the
512 ice edge and SIA (Li et al., 2017; Muilwijk et al., 2019). The Atlantic Ocean is the main heat source entering the Arctic,
513 accounting for 73 TW on average per year (Smedsrud et al., 2010), therefore an adequate simulation of the boundary
514 currents is particularly important in the Atlantic sector of the Arctic Ocean which is confirmed by the regional analysis in our
515 study. Another process that might be sensitive to horizontal ocean resolution is the Arctic river discharge, which contributes
516 both to seasonal variations of sea ice cover and long-term sea ice variability. The freshwater input stabilizes the upper ocean
517 stratification and isolates the warm Atlantic layer from the bottom of the sea ice cover (Carmack et al., 2015), resulting in
518 higher ice growth in winter. On the other hand, the heat input from the rivers accelerates sea ice melt and increases the ocean
519 temperature, which has possible implications for the next year's growing season (Park et al., 2020). The representation of

520 river discharge in HighResMIP models needs additional investigation. Our results do not show the systematic impact of
521 atmosphere resolution on the representation of the Arctic sea ice. This is confirmed by other studies reporting the minor role
522 of atmosphere resolution compared to that of the ocean (Roberts et al., 2020; Koenigk et al., 2021; Meccia et al., 2021).
523 However, increasing atmosphere resolution might permit a more realistic representation of precipitation, which can lead to
524 increased snowfall (Strandberg and Lind, 2021) and consequently invoke cooling and sea ice expansion (Bintanja et al.,
525 2018).

526 SIT is less responsive to changes in the ocean grid resolution compared to SIA and its representation largely
527 depends on the sea ice model. Our results show that in some cases large biases in SIT reduce the beneficial effect of
528 increased horizontal resolution to SIA. Poor representation of SIT is a great obstacle to the robustness of sea ice projections.
529 The high uncertainty cannot be overcome without constraining the model simulations with a sufficient number of in-situ
530 measurements of the Arctic SIT, which are still sparse and unreliable (Massonnet et al., 2018). Apart from the horizontal
531 resolution, there are other important factors affecting the model performance; for example, inaccurate representations of
532 mixed layer depth (Watts et al., 2021), surface air temperature (Papalexiou et al., 2020), surface pressure and geostrophic
533 winds (Kwok and Untersteiner, 2011; Stroeve et al., 2014), and sea ice sensitivity to global warming (Zhang, 2010). These
534 elements pair with the intrinsic complexity of sea ice models that include thermodynamics schemes and parametrizations
535 (Keen et al., 2021), sea ice dynamics components (Hunke, 2010) and coupling between the ocean and atmosphere
536 components (Hunke et al., 2020). Given few improvements with increased horizontal resolution, we argue that running the
537 models at higher resolution might not be worth the major effort of costly computations. Our results suggest that the efforts of
538 the modelling groups should be aimed rather at the improvement of the sea ice model physics and parameterizations.

539 Our analysis is limited to only one ensemble member of each model configuration, which does not allow for a
540 proper assessment of the role of internal variability. It is important to emphasize that internal variability can easily lead to
541 marked differences between the basic features of the climate models. Results from large ensembles of multidecadal
542 simulations are required to robustly quantify internal climate variability and convincingly identify deficiencies and
543 demonstrate potential progress of the climate models (e.g. Deser et al., 2020; Maher et al, 2020). Large ensembles with
544 individual CMIP-class models show that the differences between ensemble members reflect simulated internal variability.
545 For Arctic sea ice, internal variability has a large influence on multi-decadal trends (e.g., Swart et al., 2015), and has
546 reinforced anthropogenic September Arctic ice loss since 1979 (Kay et al., 2011). Using a single member or small ensembles
547 to conclude that a climate model is in error can lead to inappropriate conclusions about the model fidelity. While a large
548 number of ensemble members is desirable to account for fluctuations due to internal variability, we acknowledge that these
549 are computationally expensive and may not be always available. Unfortunately, not all HighResMIP models used in this
550 study provide multiple members. ECMWF-IFR LR, MR, and HR have 8, 3, and 6 ensemble members, respectively;
551 EC-Earth3P and CNRM have 3 ensemble members for both the LR and HR systems. Only one member is available for all
552 the other configurations. In the supplementary material, we provide additional analysis of the above-mentioned models that
553 includes all existing model members to show the weakness and robustness of the single-model response. For these three

554 models, we show SIA and SIV variability on seasonal (Figures S1, S3, and S5) and interannual (Figures S2, S4 and S6)
555 timescales, and linear SIA and SIV trends (Table S1, S2 and S3) from 1979 to 2014 for ensemble members of LR and HR
556 configurations. The minimum and maximum deviation among the “control” member for each month depict the bounds of
557 simulated internal variability. The internal variability tends to be the largest in late autumn and winters and the smallest at the
558 summer sea ice minimum when the reduced ice coverage leads to relatively low variability as seen in the seasonal cycle. The
559 magnitude of the 36-year trends in SIA and SIV is most affected, but with the small-ensemble mean generally comparable
560 with the single-member results (with the exception of CNRM ice area). Still the LR area and volume exhibit stronger
561 (weaker) negative trends than their HR counterpart in ECMWF (EC-Earth). It is worth noting that these very small ensembles
562 do not offer considerably better sampling of internal climate variability than single-model ensemble. Although the correct
563 sampling of internal variability is a necessary condition for assessing model fidelity, it is also crucial to assess how the model
564 simulates the physical mechanisms of interest. However, our analysis highlights that large ensembles of multidecadal
565 credible simulations along with strengthening the effort towards developing more realistic climate models are needed to
566 understand sea ice trends.

567 In this study, we try to understand when the Arctic will see its first ice-free summer using HighResMIP outputs.
568 Models show a wide temporal range for the occurrence of ice-free conditions in the Arctic. To reduce the inter-model spread
569 in sea ice projections we apply a widely used approach based on the selection of models according to their historical
570 performance (Wang and Overland, 2012; Sentfleben et al., 2020). Although close agreement with observations do not
571 guarantee the realism of the models, we believe that excluding the models that struggle to reproduce present-day SIA and
572 SIV mean state and trends might improve the accuracy of future sea ice projections. Different criteria to select
573 “best-performing” models exist and almost always lead to earlier near-disappearance of sea ice compared to no selection
574 (Docquier and Koenigk, 2021). The timing of the first ice-free Arctic in our model selection compares well with similar
575 criteria applied to CMIP6 models which predict the event between 2047 and 2052 while the process-based criteria advances
576 the timing of the first ice-free summer up to 2035 (Docquier and Koenigk, 2021). However, the investigation of model
577 selection criteria is out of scope of this study; our goal is to give an insight into when the Arctic might turn ice-free.

578 Our results highlight the increasing role of the MIZ in the response of Arctic sea ice to climate change. We show
579 that the MIZ will be the dominant sea ice class in the Arctic by 2050 which implies the shift to new sea ice conditions similar
580 to those in Antarctica. The chaotic interannual variability of the summer MIZF in the last years of simulations points out that
581 the current models’ physics might not be suitable to changing sea ice conditions (Figure 10). In order to realistically simulate
582 (thermo)dynamical processes, the new sea ice regime requires modifications in the models’ physics and sea ice rheology
583 which is formulated for thick pack ice (Aksenov et al., 2017). Additionally, the growing fraction of the MIZ requires changes
584 in the parameterization of the lateral and basal melt (Smith et al., 2022). The proper simulation of MIZ is essential for
585 achieving reasonable projections of future sea ice conditions since small and thin ice floes within the MIZ are more
586 vulnerable to external dynamic and thermodynamic forces than consolidated pack ice. In addition, the water patches between
587 the ice floes permit the absorption of solar radiation in the upper ocean, increasing the role of the ice-albedo effect which

588 causes anticipation of the ice-advance onset and acceleration of the overall sea ice loss. To demonstrate positive feedback
589 between summer MIZ and minimum SIA for the following year we plot the mean MIZF over June, July, August, and
590 September (JJAS) against September SIA with a 1-year lag computed for the years 2015-2050 (Figure 11a). All models
591 except one simulate negative regression ranging from $\sim -0.13 \%/10^6 \text{ km}^2$ to $-0.06 \%/10^6 \text{ km}^2$ which means that the larger
592 summer MIZF leads to lower September SIA the following year. We suggest that the MIZ might act as a predictor of future
593 sea ice conditions in the model simulations. Figure 12b shows JJAS MIZF in 2015 (start of highres-future run) against the
594 first September when the Arctic becomes ice-free. Note that not all models simulate the event before 2050. Our analysis
595 indicates that with the higher initial MIZF, the September sea ice disappears earlier. This points out that the reasonable
596 representation of the MIZ at the beginning of the run might impact the pace of sea ice loss and potentially improve the
597 accuracy of model projections. We assume that the MIZF might represent a robust criterion to examine the model fidelity.
598 The impact of the MIZ on the accuracy of the model simulations needs further investigation.

599

600 **5 Conclusions**

601 In this study, we evaluate the historical and future variability of the Arctic sea ice area and volume using six
602 coupled atmosphere-ocean general models participating in the HighResMIP experiments of the sixth phase of the Coupled
603 Model Intercomparison Project (CMIP6). For the period 1979-2014, we find that most models can properly simulate
604 maximum and minimum of the SIA seasonal cycle at hemispheric and regional scales. However, some of them cannot
605 correctly capture their magnitude, failing to realistically reproduce the ice growth and retreat phases with systematic over- or
606 underestimation of the seasonal variability. We find that the models are generally able to reproduce the seasonal cycle of the
607 Arctic-wide MIZ area, although not all of them can capture the timing of the annual maximum. The models simulate
608 different areas of the MIZ, especially in summer, however, there is stronger agreement among models for MIZF. We find
609 different regional contributions to the inter-model spread associated to seasonal variability: the winter inter-model spread in
610 SIA is attributed to the Atlantic sector (Barents-Kara Seas and the Greenland ice zones), while the summer differences are
611 tied to the the Laptev, East Siberian, and Beaufort-Chukchi Seas.

612 Selected models broadly differ on the spatial distribution of the mean SIT as well as its average values. Only few models
613 reveal a pattern similar to PIOMAS characterised by thicker ice off the coast of Greenland and the Canadian Archipelago.
614 Most models simulate too thick ice which affects the representation of sea ice volume: excluding one outlier, all but two
615 models overestimate ice volume all year round up to 1.5 times in April and 3.5 times in August. However, regardless of large
616 systematic biases, most models simulate a realistic seasonal cycle of SIV with a maximum in April and a minimum in
617 August. All models capture declines in SIA and SIV over the historical period but they disagree on the pace of sea ice loss.
618 The response to the external forcing does change with season and region: the winter trends are dominated by changes in the
619 Barents-Kara Seas and the Greenland ice zone, while the summer trends are driven by those in the East Siberian, and
620 Beaufort-Chukchi Seas. Most models underestimate ice loss in all regions particularly in summer; conversely, they tend to
621 simulate more negative trends in the Greenland zone leading to overestimating the Arctic-wide SIA trend in some

622 configurations. In this study, we find that there is no strong relationship between ocean/atmosphere resolution and sea ice
623 cover representation: the impact of horizontal resolution rather depends on the studied variable and the model used.
624 However, the ocean has a stronger effect than the atmosphere and the increase in the ocean resolution from $\sim 1^\circ$ to $\sim 0.25^\circ$
625 has a favourable impact on the representation of SIA and sea ice edges which is especially evident for ECMWF-IFS and
626 HadGEM3 models. At the same time, the simulation of SIT does not directly rely on the grid spacing, as well as the derived
627 SIV. A finer ocean resolution leads to lower SIV for ECMWF-IFS and to almost no differences for HadGEM3. Increasing
628 resolution both in ocean and atmosphere results in little difference between configurations in CNRM and higher SIV for
629 EC-Earth3P. On the other hand, enhanced atmosphere resolution leads to higher SIV for ECMWF-IFS and CMCC-CM2 and
630 lower SIV for HadGEM3 and MPI-ESM. We also find that the difference between configurations varies from one region to
631 another which highlights the importance to examine the model performance at the regional scale. For example, CMCC-CM2
632 HR4 has too low SIA and SIV in the Barents Sea caused by overestimating the OHT at the Barents Sea Opening (Docquier
633 et al., 2020) while performing well in the rest of the sectors. On the other hand, MPI-ESM has similar SIA in two
634 configurations in the Barents-Kara Seas and the Greenland ice zone, whereas the finer atmosphere configuration displays
635 less sea ice in summer in the rest of regions.

636 Considering the period 2015-2050, all models simulate a long-term decrease in SIA and SIV with a generally stronger rate of
637 ice loss compared to the historical period. Model simulations predict that the Arctic loses nearly 95% of SIV from 1950 to
638 2050. There is again no systematic impact of horizontal resolution on the occurrence of first ice-free conditions. The
639 multi-model mean of all models does not project the Arctic to become ice-free before 2050. However, applying the model
640 selection based on historical performance advances the event up to 2047. Considering that the model selection leads to closer
641 agreement with CDR on the year of first ice-free summer in the regions where it already happened (the East Siberian,
642 Barents and Kara, and the Laptev Sea), we infer that model selection application may potentially improve the accuracy of
643 model projections of Arctic sea ice evolution. Together with the overall ice shrinking, we studied the changes in the structure
644 of sea ice cover and we concluded that the MIZ will constitute up to 60-80% of the September SIA by 2050. This suggests a
645 shift to a new sea ice regime similar to that in the Antarctic. Given that the MIZ will play a major role in the response of the
646 Arctic sea ice to external forcing, modifications in the model physics and parametrizations are encouraged in the new
647 generations of coupled climate models.

648

649 **Author contributions**

650 JS analyzed the model output and observational data, and wrote the paper with contributions from all co-authors. DI
651 conceived and designed the study. All authors provided scientific input. JS and DI contributed to the conception and design of
652 this study, JS made the analysis and wrote the manuscript. FC revised the manuscript.

653 **Competing interests**

654 The contact author has declared that none of the authors has any competing interests.

655

656 **Acknowledgments**

657 JS and DI were supported by the European Union's Horizon 2020 research and innovation programme under grant agreement
658 No 101003826 via the project CRiceS. FC was supported by the Foundation Euro-Mediterranean Center on Climate Change
659 (CMCC, Italy).

660 References

- 661 Aksenov, Y., Popova, E. E., Yool, A., Nurser, A. J., Williams, T. D., Bertino, L., and Bergh, J.: On the future navigability
662 of Arctic sea routes: High-resolution projections of the Arctic Ocean and sea ice, *Marine Policy*, 75, 300–317,
663 doi:10.1016/J.MARPOL.2015.12.027, 2017.
- 664 Ärthun, M., Onarheim, I. H., Dörr, J., and Eldevik, T.: The Seasonal and Regional Transition to an Ice-Free Arctic,
665 *Geophysical Research Letters*, 48, e2020GL090825, doi:https://doi.org/10.1029/2020GL090825, 2021.
- 666 Bador, M., Boé, J., Terray, L., Alexander, L. V., Baker, A., Bellucci, A., Haarsma, R., Koenigk, T., Moine, M.-P.,
667 Lohmann, K., Putrasahan, D. A., Roberts, C., Roberts, M., Scoccimarro, E., Schiemann, R., Seddon, J., Senan, R.,
668 Valcke, S., and Vanniere, B.: Im pact of Higher Spatial Atmospheric Resolution on Precipitation Extremes Over Land
669 in Global Climate Models, *Journal of Geophysical Research: Atmospheres*, 125, e2019JD032184,
670 doi:https://doi.org/10.1029/2019JD032184, 2020.
- 671 Bintanja, R., Katsman, C. A., and Selten, F. M.: Increased Arctic precipitation slows down sea ice melt and surface
672 warming, *Oceanography*, 31, 118–125, 2018.
- 673 Brodzik, M. J. and Stewart, J. S.: Near-Real-Time SSM/I-SSMIS EASE-Grid Daily Global Ice Concentration and Snow
674 Extent, Version 5, 2016.
- 675 Carmack, E., Polyakov, I., Padman, L., Fer, I., Hunke, E., Hutchings, J., Jackson, J., Kelley, D., Kwok, R., Layton, C.,
676 Melling, H., Perovich, D., Persson, O., Ruddick, B., Timmermans, M. L., Toole, J., Ross, T., Vavrus, S., and Winsor,
677 P.: Toward quantifying the increasing role of oceanic heat in sea ice loss in the new Arctic, *Bulletin of the American
678 Meteorological Society*, 96, 2079–2105, doi:10.1175/BAMS-D-13-00177.1, 2015.
- 679 Cavalieri, D. J., Gloersen, P., and Campbell, W. J.: Determination of sea ice parameters with the NIMBUS 7 SMMR,
680 *Journal of Geophysical Research: Atmospheres*, 89, 5355–5369, doi: https://doi.org/10.1029/JD089iD04p05355, 1984.
- 681 Cherchi, A., Fogli, P. G., Lovato, T., Peano, D., Iovino, D., Gualdi, S., Masina, S., Scoccimarro, E., Materia, S., Bellucci,
682 A., and Navarra, A.: Global Mean Climate and Main Patterns of Variability in the CMCC-CM2 Coupled Model,
683 *Journal of Advances in Modeling Earth Systems*, 11, 185–209, doi:10.1029/2018MS001369, 2019.
- 684 Comiso, J. C.: Characteristics of Arctic winter sea ice from satellite multispectral microwave observations, *Journal of
685 Geophysical Research: Oceans*, 91, 975–994, doi:https://doi.org/10.1029/JC091iC01p00975, 1986.
- 686 Davy, R. and Outten, S.: The Arctic Surface Climate in CMIP6: Status and Developments since CMIP5,
687 doi:10.1175/JCLI-D-19, URL https://doi.org/10.1175/JCLI-D-19-, 2020. Dee, D. P., Uppala, S. M., Simmons, A. J.,
688 Berrisford, P., Poli, P., Kobayashi, S., Andrae, U., Balmaseda, M. A., Balsamo, G., d P Bauer, et al.: The ERA-Interim

689 reanalysis: Configuration and performance of the data assimilation system, *Quarterly Journal of the royal*
690 *meteorological society*, 137, 553–597, 2011.

691 Deser, C., Lehner, F., Rodgers, K. B., Ault, T., Delworth, T. L., DiNezio, P. N., ... & Ting, M.: Insights from Earth system
692 model initial-condition large ensembles and future prospects. *Nat. Clim. Change* 10, 277–286, 2020.

693 Docquier, D. and Koenigk, T.: Observation-based selection of climate models projects Arctic ice-free summers around
694 2035, *Communications Earth Environment*, 2, 144, doi:10.1038/s43247-021-00214-7, 2021.

695 Docquier, D., Grist, J. P., Roberts, M. J., Roberts, C. D., Semmler, T., Ponsoni, L., Mas sonnet, F., Sidorenko, D., Sein, D.
696 V., Iovino, D., Bellucci, A., and Fichet, T.: Impact of model resolution on Arctic sea ice and North Atlantic Ocean
697 heat transport, *Climate Dynamics*, 53, 4989–5017, doi:10.1007/s00382-019-04840-y, 2019.

698 Docquier, D., Fuentes-Franco, R., Koenigk, T., and Fichet, T.: Sea Ice-Ocean Interactions in the Barents Sea Modeled at
699 Different Resolutions, *Frontiers in Earth Science*, 8, doi: 10.3389/feart.2020.00172, 2020.

700 Dumont, D., Kohout, A., and Bertino, L.: A wave-based model for the marginal ice zone including a floe breaking
701 parameterization, *J. Geophys. Res.*, 116, C04 001, 2011. Eyring, V., Bony, S., Meehl, G. A., Senior, C. A., Stevens, B.,
702 Stouffer, R. J., and Taylor, K. E.: Overview of the Coupled Model Intercomparison Project Phase 6 (CMIP6)
703 experimental design and organization, *Geoscientific Model Development*, 9, 1937–1958, doi:
704 10.5194/gmd-9-1937-2016, 2016.

705 Fuentes-Franco, R. and Koenigk, T.: Sensitivity of the Arctic freshwater content and transport to model resolution,
706 *Climate Dynamics*, 53, 1765–1781, doi:10.1007/s00382-019-04735-y, 2019.

707 Grist, J. P., Josey, S. A., New, A. L., Roberts, M., Koenigk, T., and Iovino, D.: Increasing Atlantic Ocean Heat Transport
708 in the Latest Generation Coupled Ocean-Atmosphere Models: The Role of Air-Sea Interaction, *Journal of Geophysical*
709 *Research: Oceans*, 123, 8624–8637, doi:https://doi.org/10.1029/2018JC014387, 2018.

710 Haarsma, R., Acosta, M., Bakhshi, R., Bretonnière, P. A., Caron, L. P., Castrillo, M., Corti, S., Davini, P., Exarchou, E.,
711 Fabiano, F., Fladrich, U., Franco, R. F., Garcíá-Serrano, J., Hardenberg, J. V., Koenigk, T., Levine, X., Meccia, V. L.,
712 Noije, T. V., Oord, G. V. D., Palmeiro, F. M., Rodrigo, M., Ruprich-Robert, Y., Sager, P. L., Tourigny, E., Wang, S.,
713 Weele, M. V., and Wyser, K.: HighResMIP versions of EC-Earth: EC-Earth3P and EC-Earth3P-HR - Description,
714 model computational performance and basic validation, *Geoscientific Model Development*, 13, 3507–3527,
715 doi:10.5194/gmd-13-3507-2020, 2020.

716 Haarsma, R. J., Roberts, M. J., Vidale, P. L., Catherine, A., Bellucci, A., Bao, Q., Chang, P., Corti, S., Fučkar, N. S.,
717 Guemas, V., Hardenberg, J. V., Hazeleger, W., Kodama, C., Koenigk, T., Leung, L. R., Lu, J., Luo, J. J., Mao, J.,
718 Mizielinski, M. S., Mizuta, R., Nobre, P., Satoh, M., Scoccimarro, E., Semmler, T., Small, J., and Storch, J. S. V.: High
719 Resolution Model Intercomparison Project (HighResMIP v1.0) for CMIP6, *Geoscientific Model Development*, 9,
720 4185–4208, doi:10.5194/gmd-9-4185-2016, 2016.

721 Horvat, C.: Marginal ice zone fraction benchmarks sea ice and climate model skill, *Nature Communications*, 12, 2221,
722 doi:10.1038/s41467-021-22004-7, 2021.

- 723 Hunke, E.: Thickness sensitivities in the CICE sea ice model, *Ocean Modelling - OCEAN MODEL*, 34, 137–149,
724 doi:10.1016/j.ocemod.2010.05.004, 2010.
- 725 Hunke, E., Allard, R., Blain, P., Blockley, E., Feltham, D., Fichefet, T., Garric, G., Grumbine, R., Lemieux, J.-F.,
726 Rasmussen, T., Ribergaard, M., Roberts, A., Schweiger, A., Tietsche, S., Tremblay, B., Vancoppenolle, M., and Zhang,
727 J.: Should sea ice Modeling Tools Designed for Climate Research Be Used for Short-Term Forecasting?, *Current*
728 *Climate Change Reports*, 6, 121–136, doi:10.1007/s40641-020-00162-y, 2020.
- 729 Ivanova, N., Pedersen, L. T., Tonboe, R. T., Kern, S., Heygster, G., Lavergne, T., Sørensen, A., Saldo, R., Dybkjær, G.,
730 Brucker, L., and Shokr, M.: Inter-comparison and evaluation of sea ice algorithms: towards further identification of
731 challenges and optimal approach using passive microwave observations, *The Cryosphere*, 9, 1797–1817,
732 doi:10.5194/tc-9-1797-2015, 2015.
- 733 Jackson, L. C., Roberts, M. J., Hewitt, H. T., Iovino, D., Koenigk, T., Meccia, V. L., Roberts, C. D., Ruprich-Robert, Y.,
734 and Wood, R. A.: Impact of ocean resolution and mean state on the rate of AMOC weakening, *Climate Dynamics*, 55,
735 1711–1732, doi: 10.1007/s00382-020-05345-9, 2020.
- 736 Jungclaus, J. H., Fischer, N., Haak, H., Lohmann, K., Marotzke, J., Matei, D., Mikolajewicz, U., Notz, D., and Storch, J.
737 S. V.: Characteristics of the ocean simulations in the Max Planck Institute Ocean Model (MPIOM) the ocean
738 component of the MPI-Earth system model, *Journal of Advances in Modeling Earth Systems*, 5, 422–446,
739 doi:10.1002/jame.20023, 2013.
- 740 Kalnay, E., Kanamitsu, M., Kistler, R., Collins, W., Deaven, D., Gandin, L., Iredell, M., Saha, S., White, G., Woollen, J.,
741 Zhu, Y., Chelliah, M., Ebisuzaki, W., Higgins, W., Janowiak, J., Mo, K. C., Ropelewski, C., Wang, J., Leetmaa, A.,
742 Reynolds, R., Jenne, R., and Joseph, D.: The NCEP/NCAR 40-Year Reanalysis Project, *Bulletin of the American*
743 *Meteorological Society*, 77, 437 – 472, doi:10.1175/1520-0477(1996)077<0437:TNYRPP>2.0.CO;2, 1996.
- 744 Kay, J. E., Holland, M. M, and Jahn, A.: Inter-annual to multi-decadal Arctic sea ice extent trends in a warming world,
745 *Geophys. Res. Lett.*, 38, L15708, doi:10.1029/2011GL048008, 2011.
- 746 Keen, A., Blockley, E., Bailey, D. A., Debernard, J. B., Bushuk, M., Delhay, S., Docquier, D., Feltham, D., Massonnet,
747 F., O’Farrell, S., Ponsoni, L., Rodriguez, J. M., Schroeder, D., Swart, N., Toyoda, T., Tsujino, H., Vancoppenolle, M.,
748 and Wyser, K.: An inter-comparison of the mass budget of the Arctic sea ice in CMIP6 models, *The Cryosphere*, 15,
749 951–982, doi:10. 5194/tc-15-951-2021, 2021.
- 750 Koenigk, T., Fuentes-Franco, R., Meccia, V. L., Gutjahr, O., Jackson, L. C., New, A. L., Ortega, P., Roberts, C. D.,
751 Roberts, M. J., Arsouze, T., Iovino, D., Moine, M. P., and Sein, D. V.: Deep mixed ocean volume in the Labrador Sea
752 in HighResMIP models, *Climate Dynamics*, 57, 1895–1918, doi:10.1007/s00382-021-05785-x, 2021.
- 753 Kwok, R. and Untersteiner, N.: The thinning of Arctic sea ice, *Physics Today*, 64, 36–41, doi: 10.1063/1.3580491, 2011.
- 754 Labe, Z., Magnusdottir, G., and Stern, H.: Variability of Arctic Sea Ice Thickness Using PIOMAS and the CESM Large
755 Ensemble, *Journal of Climate*, 31, 3233 – 3247, doi: 10.1175/JCLI-D-17-0436.1, 2018.
- 756 Lavergne, T., Sørensen, A. M., Kern, S., Tonboe, R., Notz, D., Aaboe, S., Bell, L., Dybkjær, G., Eastwood, S., Gabarro,

757 C., Heygster, G., Killie, M. A., Kreiner, M. B., Lavelle, J., Saldo, R., Sandven, S., and Pedersen, L. T.: Version 2 of the
758 EUMETSAT OSI SAF and ESA CCI sea ice concentration climate data records, *The Cryosphere*, 13, 49–78,
759 doi:10.5194/tc-13-49-2019, 2019.

760 Li, D., Zhang, R., and Knutson, T. R.: On the discrepancy between observed and CMIP5 multi-model simulated Barents
761 Sea winter sea ice decline, *Nature Communications*, 8, 14 991, doi:10.1038/ncomms14991, 2017.

762 Lohmann, K., Putrasahan, D. A., von Storch, J.-S., Gutjahr, O., Jungclaus, J. H., and Haak, H.: Response of Northern
763 North Atlantic and Atlantic Meridional Overturning Circulation to Reduced and Enhanced Wind Stress Forcing,
764 *Journal of Geophysical Research: Oceans*, 126, e2021JC017 902, doi:https://doi.org/10.1029/2021JC017902, 2021.

765 Madec, G., Bourdallé-Badie, R., Chanut, J., Clementi, E., Coward, A., Ethé, C., Iovino, D., Lea, D., Lévy, C., Lovato, T.,
766 Martin, N., Masson, S., Mocavero, S., Rousset, C., Storkey, D., Müeller, S., Nurser, G., Bell, M., Samson, G., Mathiot,
767 P., Mele, F., and Moulin, A.: NEMO ocean engine, doi:10.5281/ZENODO.6334656, 2016.

768 Maher, N., Lehner, F., and Marotzke, J.: Quantifying the role of internal variability in the temperature we expect to
769 observe in the coming decades. *Environ. Res. Lett.* 15, 054014, 2020.

770 Massonnet, F., Vancoppenolle, M., Goosse, H., Docquier, D., Fichet, T., and Blanchard Wrigglesworth, E.: Arctic sea
771 ice change tied to its mean state through thermodynamic processes, *Nature Climate Change*, 8, 599–603,
772 doi:10.1038/s41558-018-0204-z, 2018.

773 Meccia, V. L., Iovino, D., and Bellucci, A.: North Atlantic gyre circulation in PRIMAVERA models, *Climate Dynamics*,
774 56, 4075–4090, doi:10.1007/s00382-021-05686-z, 2021.

775 Meier, WN, Stroeve, J and Fetterer, F. Whither Arctic sea ice? A clear signal of decline regionally, seasonally and extending
776 beyond the satellite record. *Ann. Glaciol.*, 46, 428–434. doi: 10.3189/172756407782871170, 2007

777 Meier, W. N., Peng, G., Scott, D. J., and Savoie, M. H. Verification of a New NOAA/NSIDC Passive Microwave sea ice
778 Concentration Climate Record. *Polar Res.* 33 (1), 21004. doi:10.3402/polar.v33.21004, 2014.

779 Meier, W. N., Fetterer, F., Windnagel, A. K., and Stewart, J. S.: NOAA/NSIDC Climate Data Record of Passive
780 Microwave Sea Ice Concentration, Version 4, doi:10.7265/efmz-2t65, 2021.

781 Muilwijk, M., Ilicak, M., Cornish, S. B., Danilov, S., Gelderloos, R., Gerdes, R., Haid, V., Haine, T. W. N., Johnson, H.
782 L., Kostov, Y., Kovács, T., Lique, C., Marson, J. M., Myers, P. G., Scott, J., Smedsrud, L. H., Talandier, C., and Wang,
783 Q.: Arctic Ocean Response to Greenland Sea Wind Anomalies in a Suite of Model Simulations, *Journal of*
784 *Geophysical Research: Oceans*, 124, 6286–6322, doi:https://doi.org/10.1029/2019JC015101, 2019.

785 Müller, W. A., Jungclaus, J. H., Mauritsen, T., Baehr, J., Bittner, M., Budich, R., Bunzel, F., Esch, M., Ghosh, R., Haak,
786 H., Ilyina, T., Kleine, T., Kornblueh, L., Li, H., Modali, K., Notz, D., Pohlmann, H., Roeckner, E., Stemmler, I., Tian,
787 F., and Marotzke, J.: A Higher-resolution Version of the Max Planck Institute Earth System Model (MPI-ESM1.2-HR),
788 *Journal of Advances in Modeling Earth Systems*, 10, 1383–1413, doi:10.1029/2017MS001217, 2018.

789 Notz, D. and Community, S.: Arctic Sea Ice in CMIP6, *Geophysical Research Letters*, 47, e2019GL086749,
790 doi:https://doi.org/10.1029/2019GL086749, 2020.

791 Notz, D. and Stroeve, J.: Observed Arctic sea ice loss directly follows anthropogenic CO₂ emission, *Science*, 354,
792 747–750, doi:10.1126/science.aag2345, 2016.

793 Onarheim, I. H., Eldevik, T., Smedsrud, L. H., and Stroeve, J. C.: Seasonal and Regional Manifestation of Arctic Sea Ice
794 Loss, *Journal of Climate*, 31, 4917 – 4932, doi: 10.1175/JCLI-D-17-0427.1, 2018.

795 Ono, J., Komuro, Y., and Tatebe, H.: Impact of sea ice thickness initialized in April on Arctic sea ice extent predictability
796 with the MIROC climate model, *Annals of Glaciology*, 61, 97–105, doi:10.1017/aog.2020.13, 2020.

797 Papalexiou, S. M., Rajulapati, C. R., Clark, M. P., and Lehner, F.: Robustness of CMIP6 Historical Global Mean
798 Temperature Simulations: Trends, Long-Term Persistence, Auto correlation, and Distributional Shape, *Earth’s Future*,
799 8, e2020EF001 667, doi:https://doi.org/10.1029/2020EF001667, 2020.

800 Park, H., Watanabe, E., Kim, Y., Polyakov, I., Oshima, K., Zhang, X., Kimball, J. S., and Yang, D.: Increasing riverine
801 heat influx triggers Arctic sea ice decline and oceanic and atmospheric warming, *Science Advances*, 6, eabc4699,
802 doi:10.1126/sciadv.abc4699, URL <https://www.science.org/doi/abs/10.1126/sciadv.abc4699>, 2020.

803 Parkinson, CL, Cavalieri, DJ, Gloersen, P, Zwally, HJ and Comiso, JC. Arctic sea ice extents, areas, and trends, 1978–1996.
804 *J. Geophys. Res.*, 104(C9), 20,837–20,856, 1999.

805 Paul, F., Mielke, T., Schwarz, C., Schröder, J., Rampai, T., Skatulla, S., Audh, R. R., Hepworth, E., Vichi, M., and
806 Lupascu, D. C.: Frazil Ice in the Antarctic Marginal Ice Zone, *Journal of Marine Science and Engineering*, 9,
807 doi:10.3390/jmse9060647, URL <https://www.mdpi.com/2077-1312/9/6/647>, 2021.

808 Peng, G., and Meier, W.: Temporal and regional variability of Arctic sea ice coverage from satellite data, *Annals of*
809 *Glaciology*, 59, 76pt2, 191-200. doi:10.1017/aog.2017.32, 2018.

810 Perovich, D., Meier, W., Tschudi, M., Hendricks, S., Petty, A. A., Divine, D., Farrell, S., Gerland, S., Haas, C., Kaleschke,
811 L., Pavlova, O., Ricker, R., Tian-Kunze, X., Webster, M., and Wood, K.: NOAA Arctic Report Card 2020,
812 doi:10.25923/n170-9h57, 2020.

813 Roberts, C. D., Senan, R., Molteni, F., Boussetta, S., Mayer, M., and Keeley, S. P.: Climate model configurations of the
814 ECMWF integrated forecasting system (ECMWF-IFS cycle43r1) for HighResMIP, *Geoscientific Model Development*,
815 11, 3681–3712, doi:10.5194/ gmd-11-3681-2018, 2018.

816 Roberts, M. J., Jackson, L. C., Roberts, C. D., Meccia, V., Docquier, D., Koenigk, T., Ortega, P., Moreno-Chamarro, E.,
817 Bellucci, A., Coward, A., Drijfhout, S., Exarchou, E., Gutjahr, O., Hewitt, H., Iovino, D., Lohmann, K., Putrasahan,
818 D., Schiemann, R., Seddon, J., Terray, L., Xu, X., Zhang, Q., Chang, P., Yeager, S. G., Castruccio, F. S., Zhang, S., and
819 Wu, L.: Sensitivity of the Atlantic Meridional Overturning Circulation to Model Resolution in CMIP6 HighResMIP
820 Simulations and Implications for Future Changes, *Journal of Advances in Modeling Earth Systems*, 12,
821 doi:10.1029/2019MS002014, 2020.

822 Rolph, R. J., Feltham, D. L., and Schröder, D.: Changes of the Arctic marginal ice zone during the satellite era, *The*
823 *Cryosphere*, 14, 1971–1984, doi:10.5194/tc-14-1971-2020, 2020.

824 Senfleben, D., A. Lauer, and A. Karpechko: Constraining Uncertainties in CMIP5 Projections of September Arctic Sea Ice
825 Extent with Observations. *J. Climate*, 33, 1487–1503, <https://doi.org/10.1175/JCLI-D-19-0075.1>, 2020.

826 Serreze, M. C. and Meier, W. N.: The Arctic's sea ice cover: trends, variability, predictability, and comparisons to the
827 Antarctic, *Annals of the New York Academy of Sciences*, 1436, 36–53, doi:10.1111/nyas.13856, 2019.

828 Shu, Q., Wang, Q., Song, Z., Qiao, F., Zhao, J., Chu, M., and Li, X.: Assessment of Sea Ice Extent in CMIP6 With
829 Comparison to Observations and CMIP5, *Geophysical Research Letters*, 47, e2020GL087965,
830 doi:<https://doi.org/10.1029/2020GL087965>, 2020.

831 Smedsrud, L. H., Ingvaldsen, R., Nilsen, J. E. Ø., and Skagseth, Ø.: Heat in the Barents Sea: transport, storage, and
832 surface fluxes, *Ocean Science*, 6, 219–234, doi:10.5194/os-6-219-2010, 2010.

833 Smith, M. M., von Albedyll, L., Raphael, I. A., Lange, B. A., Matero, I., Salganik, E., Webster, M. A., Granskog, M. A.,
834 Fong, A., Lei, R., and Light, B.: Quantifying false bottoms and under-ice meltwater layers beneath Arctic summer sea
835 ice with fine-scale observations, *Elementa: Science of the Anthropocene*, 10, 000116,
836 doi:10.1525/elementa.2021.000116, 2022.

837 Strandberg, G. and Lind, P.: The importance of horizontal model resolution on simulated precipitation in Europe – from
838 global to regional models, *Weather and Climate Dynamics*, 2, 181–204, doi:10.5194/wcd-2-181-2021, 2021.

839 Stroeve, J., Barrett, A., Serreze, M., and Schweiger, A.: Using records from submarine, aircraft and satellites to evaluate
840 climate model simulations of Arctic sea ice thickness, *The Cryosphere*, 8, 1839–1854, doi:10.5194/tc-8-1839-2014,
841 2014.

842 Strong, C., Foster, D., Cherkaev, E., Eisenman, I., and Golden, K. M.: On the Definition of Marginal Ice Zone Width, *J.*
843 *Atmos. Ocean. Tech.*, 34, 1565–1584, <https://doi.org/10.1175/JTECH-D-16-0171.1>, 2017.

844 Swart, N. C., Fyfe, J. C., Hawkins, E., Kay, J. E., and Jahn, A.: Influence of internal variability on Arctic sea-ice trends.
845 *Nature Climate Change*, 5, 86–89. doi:10.1038/nclimate2483, 2015.

846 Tápias, G., Lizotte, M., Kieber, M., D. Randelhoff, A., Xue, R., Dinasquet, L., Babin, J., Rehm, M., and Levasseur, E.:
847 DMS emissions from the Arctic marginal ice zone, *Elementa: Science of the Anthropocene*, 9,
848 doi:10.1525/elementa.2020.00113, 2021.

849 Voldoire, A., Saint-Martin, D., Sénési, S., Decharme, B., Alias, A., Chevallier, M., Colin, J., Guérémy, J. F., Michou, M.,
850 Moine, M. P., Nabat, P., Roehrig, R., y Méliá, D. S., Séférian, R., Valcke, S., Beau, I., Belamari, S., Berthet, S.,
851 Cassou, C., Cattiaux, J., Deshayes, J., Douville, H., Ethé, C., Franchistéguy, L., Geoffroy, O., Lévy, C., Madec, G.,
852 Meurdesoif, Y., Msadek, R., Ribes, A., Sanchez-Gomez, E., Terray, L., and Waldman, R.: Evaluation of CMIP6 DECK
853 Experiments With CNRM-CM6-1, *Journal of Advances in Modeling Earth Systems*, 11, 2177–2213,
854 doi:10.1029/2019MS001683, 2019.

855 Wadhams, P. and Deacon, G. E. R.: Sea-ice topography of the Arctic Ocean in the region 70° W to 25° E, *Philosophical*
856 *Transactions of the Royal Society of London. Series A, Mathematical and Physical Sciences*, 302, 45–85,
857 doi:10.1098/rsta.1981.0157, 1981.

858 Wang, M., and Overland, J. E.: A sea ice free summer Arctic within 30 years: An update from CMIP5 models, *Geophys.*
859 *Res. Lett.*, 39, L18501, doi:10.1029/2012GL052868, 2020.

860 Wang, X., Key, J., Kwok, R., and Zhang, J.: Comparison of Arctic sea ice thickness from satellites, aircraft, and PIOMAS
861 data, *Remote Sensing*, 8, doi:10.3390/RS8090713, 2016. Watts, M., Maslowski, W., Lee, Y. J., Kinney, J. C., and
862 Osinski, R.: A Spatial Evaluation of Arctic Sea Ice and Regional Limitations in CMIP6 Historical Simulations, *Journal*
863 *of Climate*, 34, 6399–6420, doi:10.1175/JCLI-D-20-0491.1, 2021.

864 Williams, K. D., Copsey, D., Blockley, E. W., Bodas-Salcedo, A., Calvert, D., Comer, R., Davis, P., Graham, T., Hewitt,
865 H. T., Hill, R., Hyder, P., Ineson, S., Johns, T. C., Keen, A. B., Lee, R. W., Megann, A., Milton, S. F., Rae, J. G. L.,
866 Roberts, M. J., Scaife, A. A., Schiemann, R., Storkey, D., Thorpe, L., Watterson, I. G., Walters, D. N., West, A., Wood,
867 R. A., Woollings, T., and Xavier, P. K.: The Met Office Global Coupled Model 3.0 and 3.1 (GC3.0 and GC3.1)
868 Configurations, *Journal of Advances in Modeling Earth Systems*, 10, 357–380,
869 doi:https://doi.org/10.1002/2017MS001115, 2018.

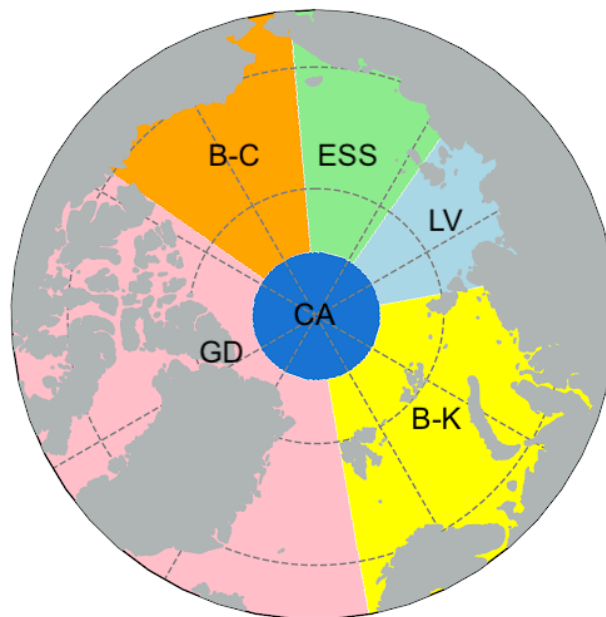
870 Zhang, J. and Rothrock, D. A.: Modeling Global Sea Ice with a Thickness and Enthalpy Distribution Model in
871 Generalized Curvilinear Coordinates, 2003.

872 Zhang, X.: Sensitivity of Arctic Summer Sea Ice Coverage to Global Warming Forcing: Toward Reducing Uncertainty in
873 Arctic Climate Change Projections, *Tellus A*, 62, 220 – 227, doi: 10.1111/j.1600-0870.2010.00441.x, 2010.

874

875 **Figures**

876



877

878

879 **Figure 1: Map of sub-regions used in the regional analysis: Central Arctic Basin (CA), Barents and Kara Seas (B-K), Laptev Sea**
880 **(LV), East Siberian Sea (ESS), Beaufort and Chukchi Seas (B-C), Canadian Arctic Archipelago and Greenland coast (GD).**

881

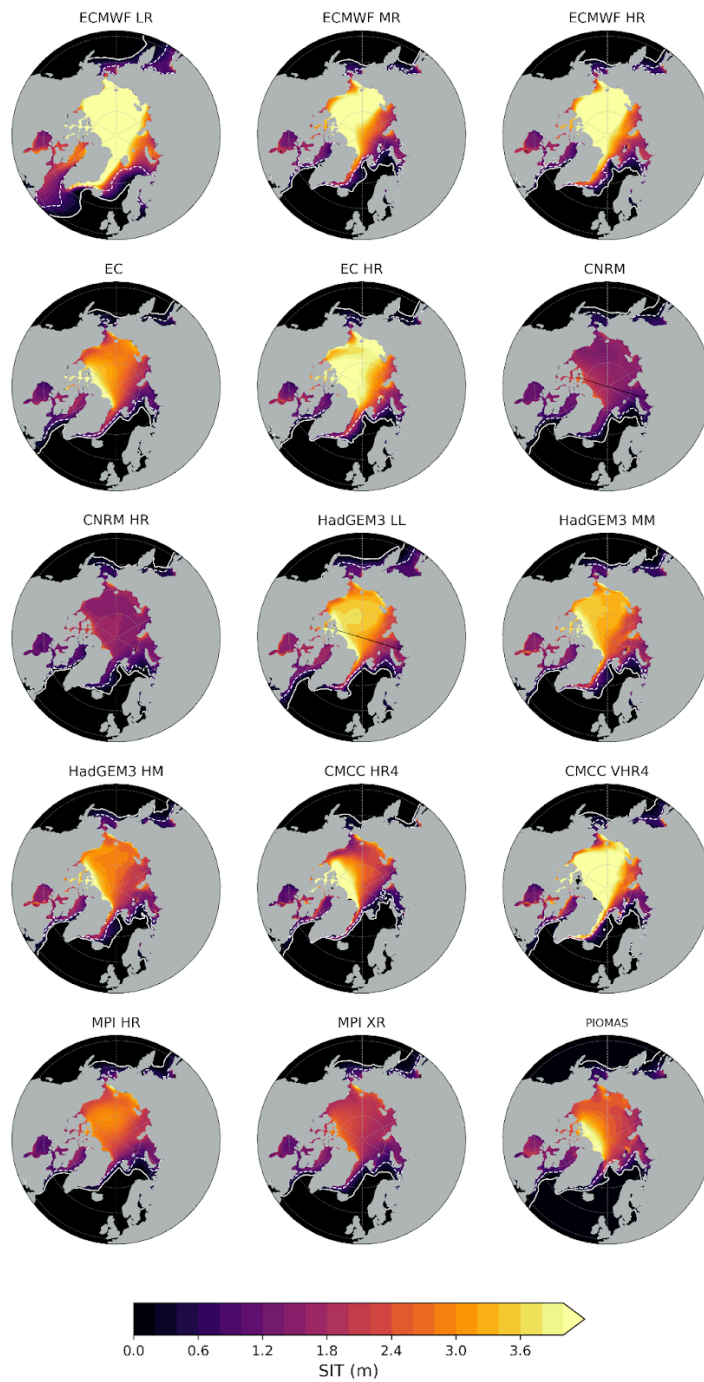
882

883

884

885

886 **a)**

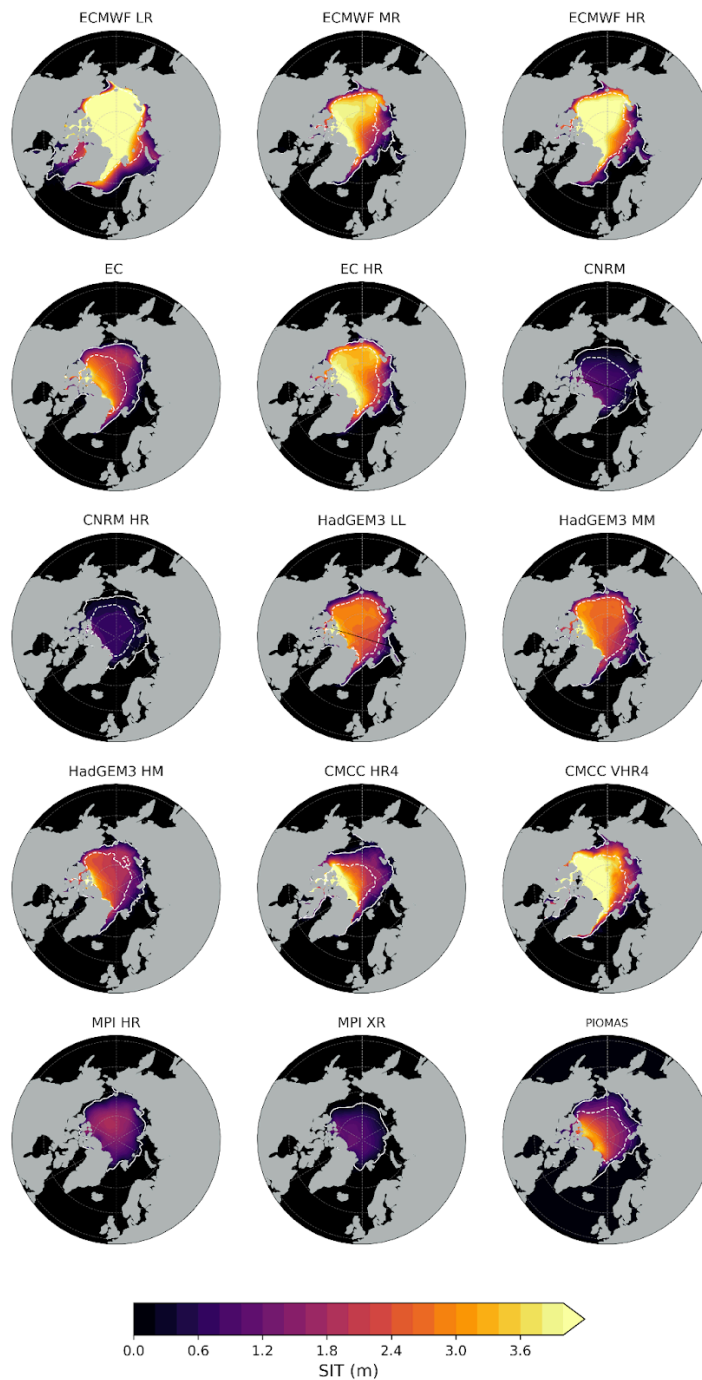


887

888

889

890 b)

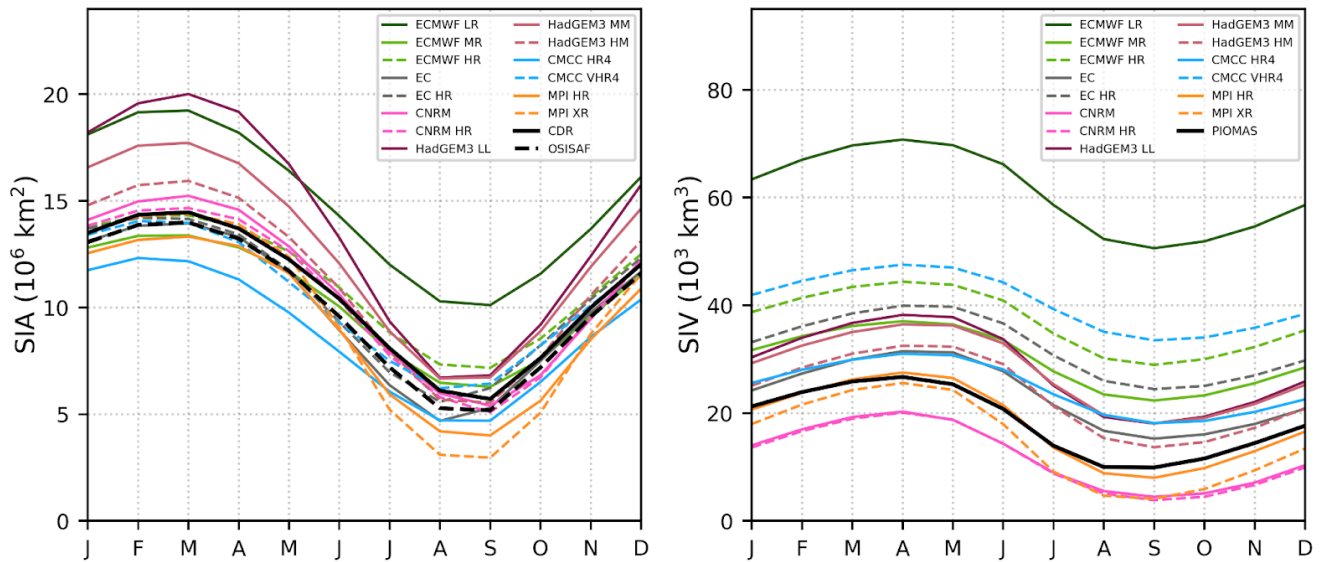


891

892 Figure 2: The 1979-2014 climatological mean sea ice thickness from the model outputs and PIOMAS in March (a) and September
 893 (b). White contours show the edges of 15% (solid) and 80% (dashed) sea ice concentration from each model. SIC from CDR is used
 894 for PIOMAS.

895 (a)

(b)



896

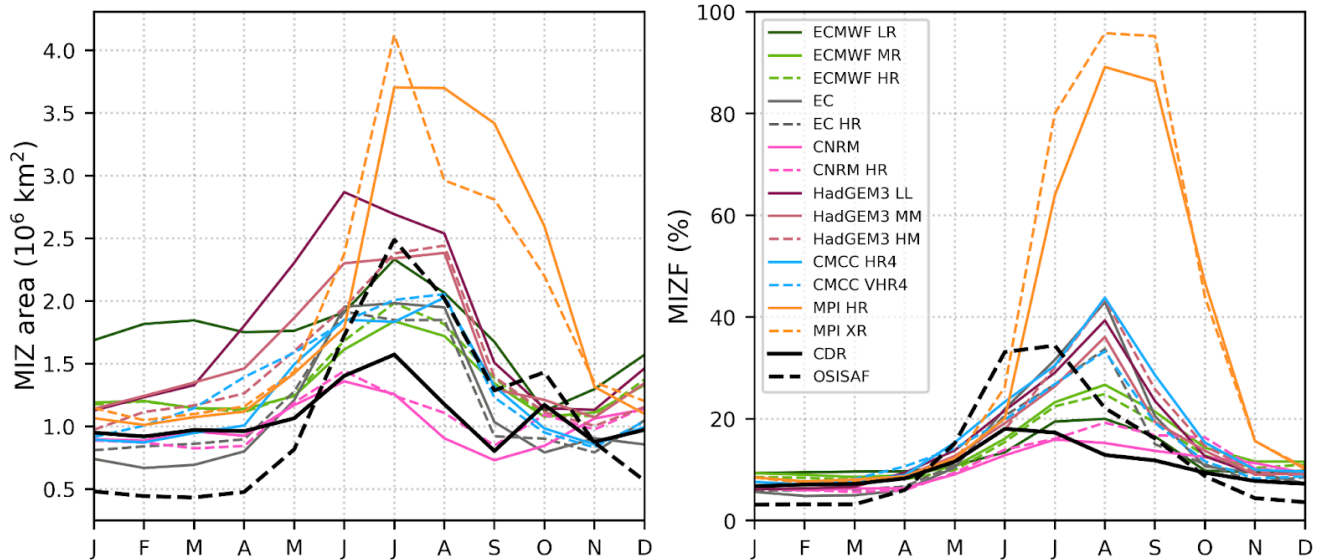
897 **Figure 3: The 1979-2014 seasonal cycle in SIA (a) and SIV (b) from HighResMIP hist-1950 model outputs against CDR and**
 898 **OSISAF for SIA and PIOMAS for SIV.**

899

900

(a)

(b)

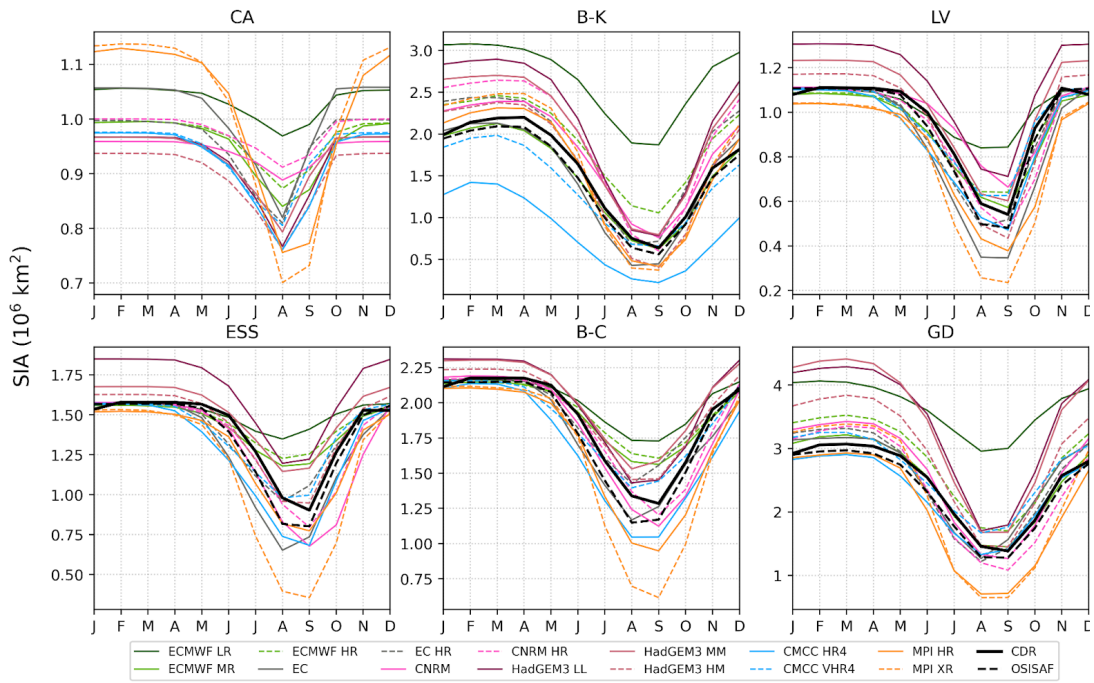


901

902 **Figure 4: The 1979-2014 seasonal cycle in the MIZ area (a) and MIZF (b) from HighResMIP hist-1950 model outputs and**
 903 **satellite products.**

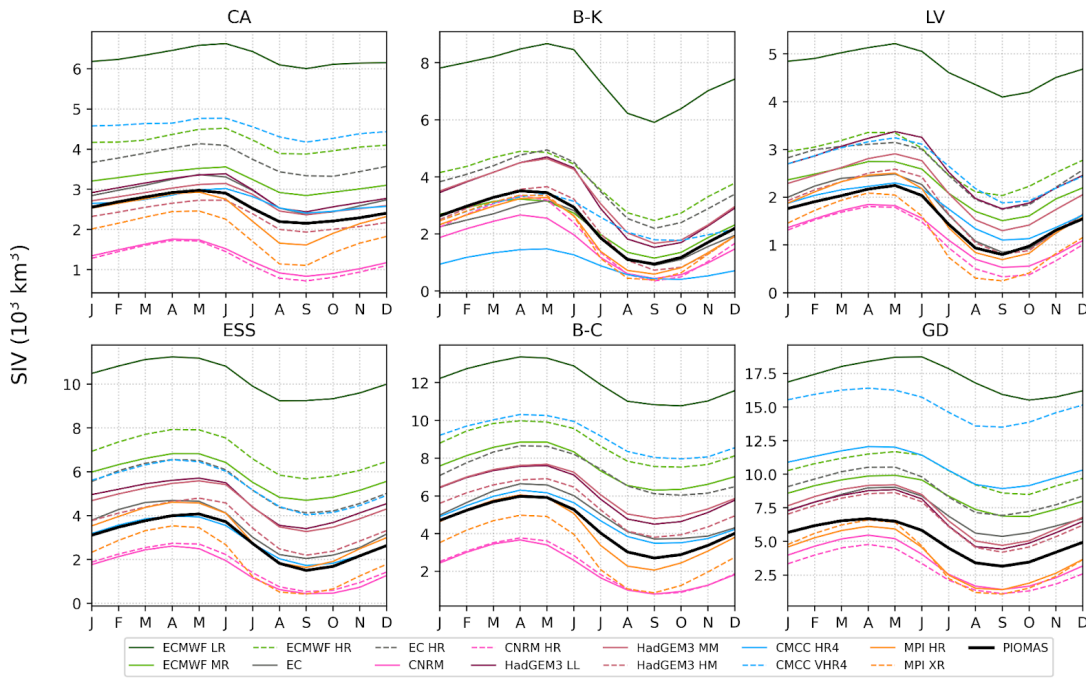
904

(a)



905

906 b)



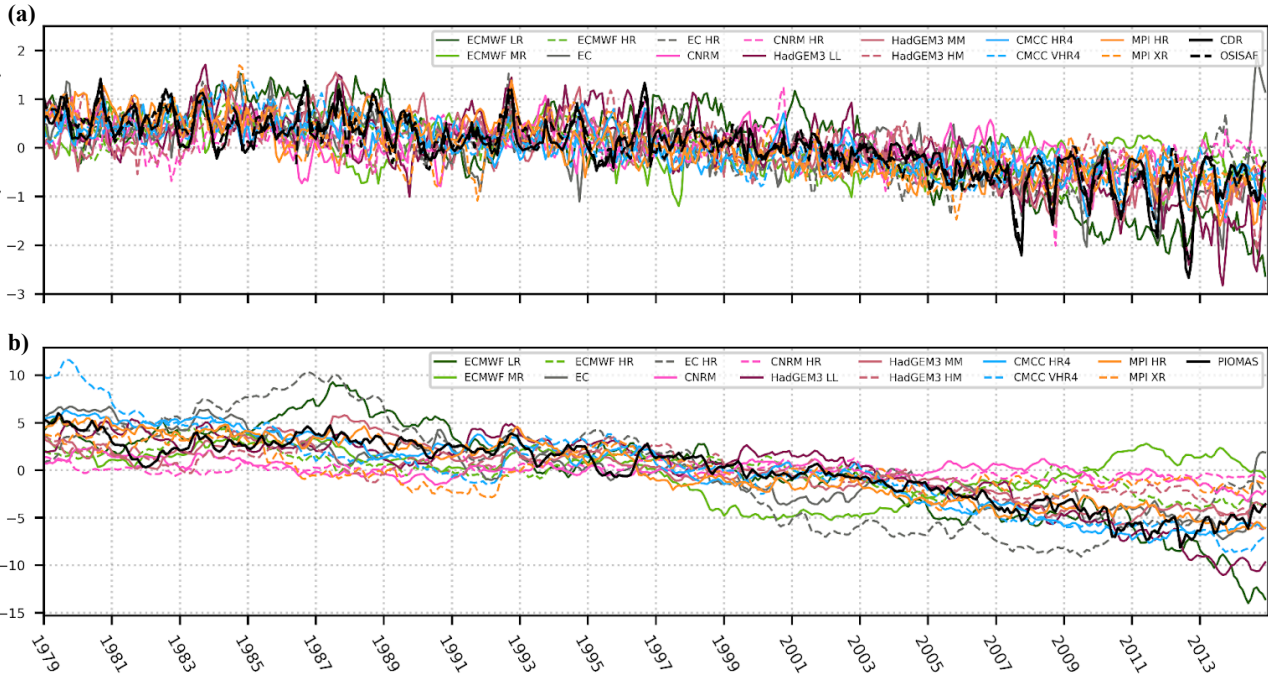
907

908 **Figure 5: The 1979-2014 seasonal cycle in a) SIA and b) SIV in the Arctic sub-regions from HighResMIP hist-1950 model**
 909 **outputs against CDR and OSISAF for SIA and PIOMAS for SIV.**

910

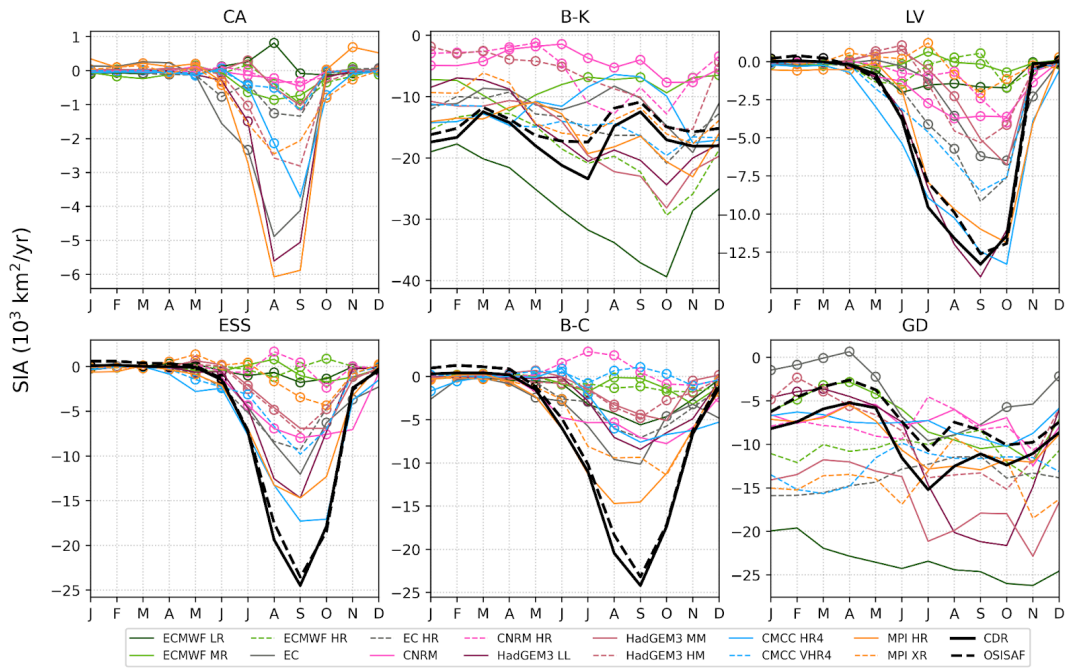
911
912
913
914
915
916
917
918
919
920
921
922

923
924
925
926
927
928
929
930
931
932
933
934



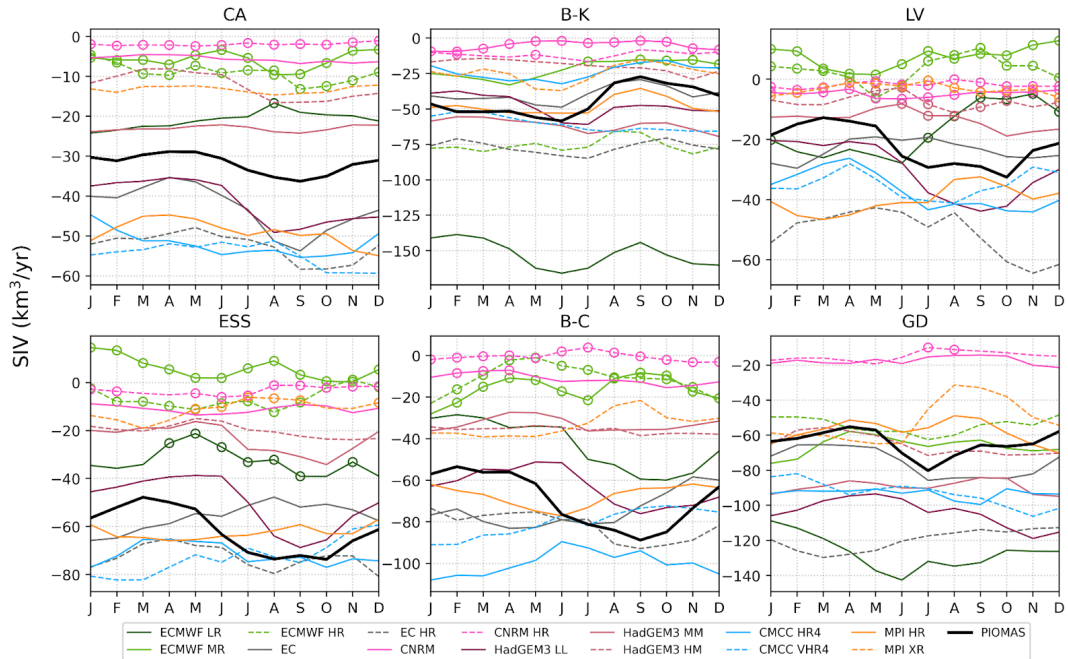
935 **Figure 6: Monthly anomalies of SIA (a) and SIV (b) over 1979-2014 from HighResMIP model outputs and reference products.**

958 (a)



959

960 b)

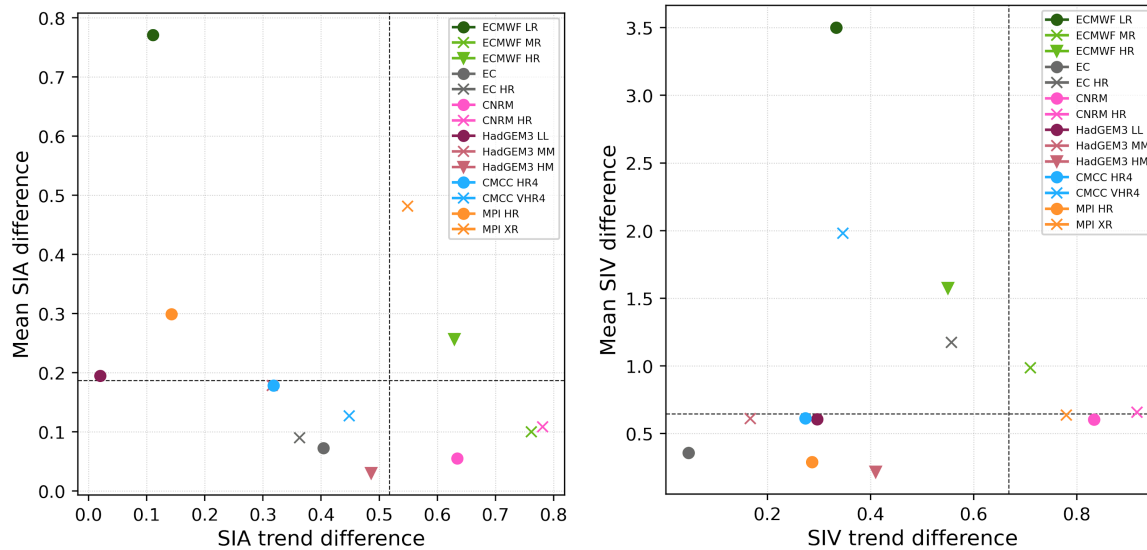


961

962 Figure 7: The 1979-2014 monthly trends in SIA (a) and SIV (b) in the Arctic sub-regions for HighResMIP hist-1950 model outputs
 963 against CDR and OSISAF for SIA and PIOMAS for SIV. Dots indicate non-significant trends.

964 (a)

(b)

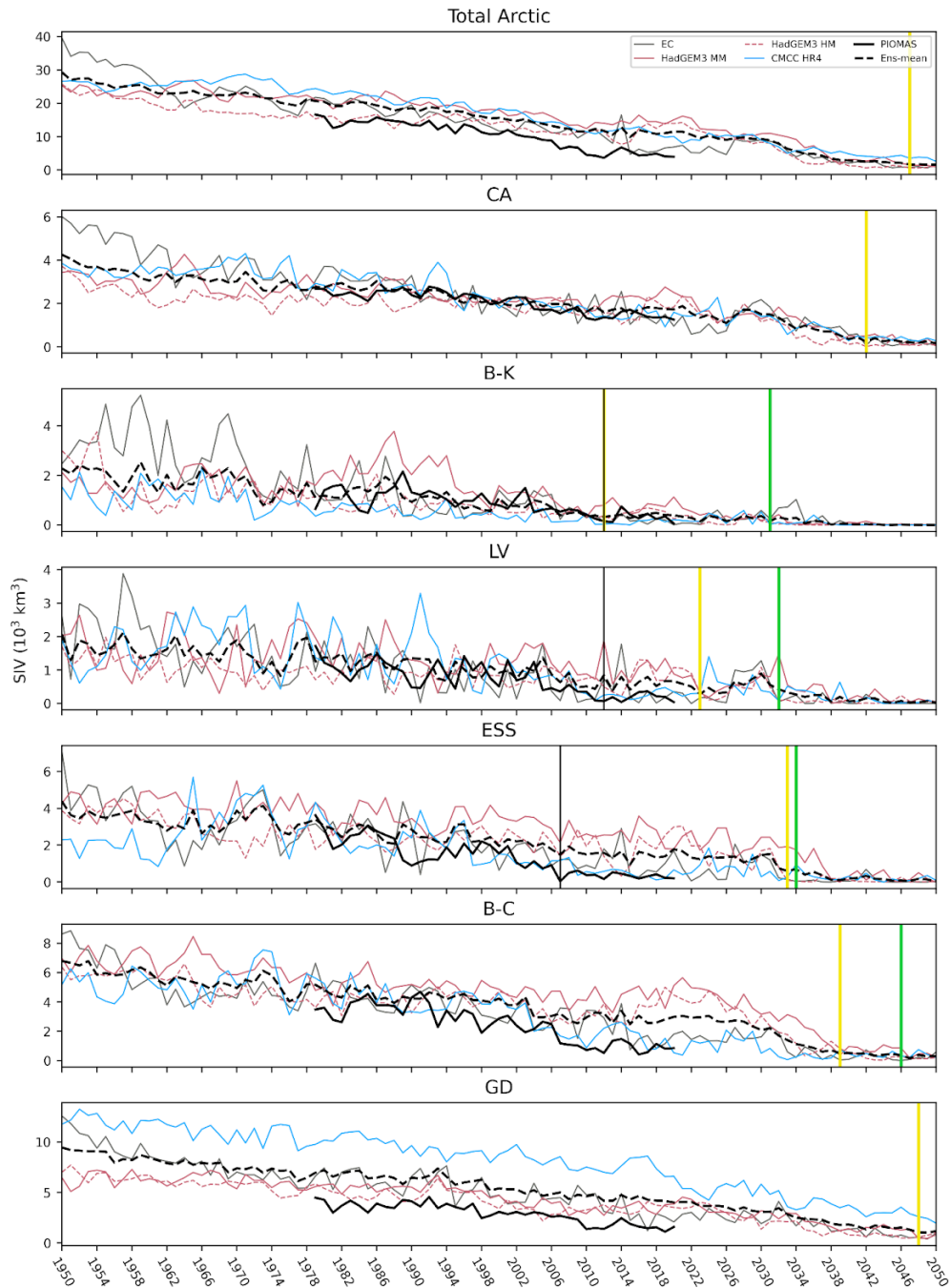


965

966 **Figure 8. Normalized difference in mean September SIA against September SIA trend over 1979-2014 (a). Same for SIV (b).**

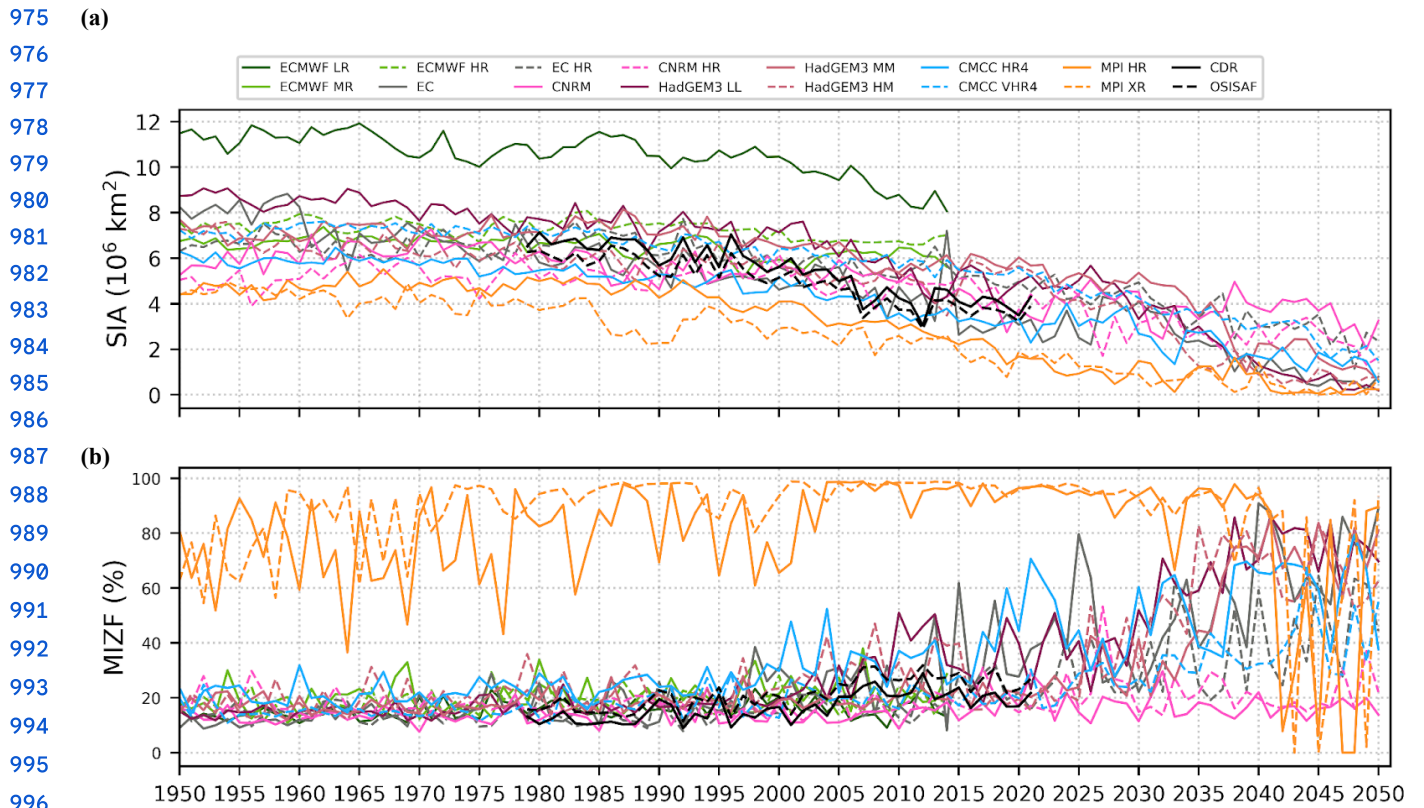
967 **The difference is computed with reference to CDR (for SIA) and PIOMAS (for SIV). Dashed lines indicate 75th percentile for a**

968 **set of the model outputs excluding ECMWF-IFS.**



969

970 **Figure 9: Time series of September SIV from 1950 to 2050 using HighResMIP historical and future runs and PIOMAS for the**
 971 **entire Arctic and sub-regions. The multi-model mean SIV with model selection is shown by dashed line. The vertical lines**
 972 **indicate the time of ice-free conditions: green colour for the multi-model mean without model selection, yellow for the**
 973 **multi-model mean with model selection, and black for CDR. Free-ice conditions signify that SIA falls below 10^6 km^2 for the**
 974 **total Arctic and reaches 25% of the CDR SIA averaged over 1980-2010 for the sub-regions.**

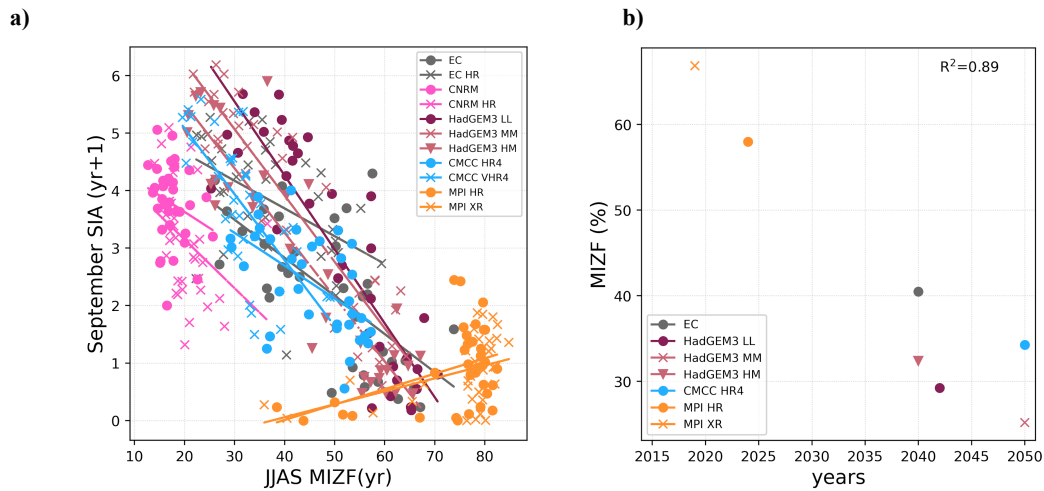


997 **Figure 10: Time series of September SIA (a) and MIZF (b) from 1950 to 2050 using HighResMIP historical and future runs and**
 998 **satellite products (CDR and OSISAF).**

999

1000

1001



1002 **Figure 11: June, July, August, and September (JJAS) MIZF mean against September SIA with one year lag over 2015-2050 (a);**
 1003 **Timing of first ice-free Arctic against JJAS MIZF in 2015 (b).**
 1004